Observing a Light Dark Matter Beam With Neutrino Experiments

by

Patrick deNiverville
B.Sc., Mount Allison University, 2009

A Thesis Submitted in Partial Fulfillment of the
Requirements for the Degree of

MASTER OF SCIENCE

in the Department of Physics and Astronomy

Observing a Light Dark Matter Beam With Neutrino Experiments

by

Patrick deNiverville
B.Sc., Mount Allison University, 2009

Supervisory Committee

Dr. A. Ritz, Supervisor
(Department of Physics and Astronomy)

Dr. P. Kovtun, Departmental Member
(Department of Physics and Astronomy)

Supervisory Committee

Dr. A. Ritz, Supervisor
(Department of Physics and Astronomy)

Dr. P. Kovtun, Departmental Member
(Department of Physics and Astronomy)

ABSTRACT

We consider the sensitivity of high luminosity neutrino experiments to light stable states, as arise in scenarios of MeV-scale dark matter. To ensure the correct thermal relic abundance, such states must annihilate to the Standard model via light mediators, providing a portal for access to the dark matter state in colliders or fixed targets. This framework implies that neutrino beams produced at a fixed target will also carry an additional dark matter beam, which can mimic neutrino scattering off electrons or nuclei in the detector. We therefore develop a Monte Carlo code to simulate the production of a dark matter beam at two proton fixed-target facilities with high luminosity, LSND and MiniBooNE, and with this simulation determine the existing limits on light dark matter. We find in particular that MeV-scale dark matter scenarios motivated by an explanation of the galactic 511 keV line are strongly constrained.

Contents

List of Figures

ACKNOWLEDGEMENTS

I would like to thank:

my parents, Bill and Germaine deNiverville, for their constant support, encouragement and advice throughout my years of higher education.

Dr. Adam Ritz, for his fantastic teaching, providing direction, encouragement and aid in research, and patiently answering my many questions.

NSERC, for their generous monetary support of education and student research through both undergraduate and graduate scholarships.

University of Victoria and the Department of Physics and Astronomy, for providing generous monetary support, excellent classes, and space in which to work and learn.

Chapter 1

Introduction

Dark matter stands as one of the greatest mysteries of modern physics and cosmology. There is overwhelming evidence for its existence from both astrophysical and cosmological sources, and the ability of the dark matter hypothesis to tie together many disparate threads of evidence makes it very difficult to ignore. We have labeled a large majority of the matter content of the Universe as dark matter, but we have no knowledge of its true particle content. We do not know if it is made up of a single species of matter or a dozen, nor can we say how it interacts, if at all, with the much rarer Standard Model particles that we have become increasingly familiar with over the last century. Taken together, these considerations have made dark matter an exciting and active area of research, as well as an important motivator of new physics theories and searches.

The paradigm of the electroweak-scale Weakly Interacting Massive Particle (WIMP) provides a simple and compelling explanation for the particle content of dark matter, and has served as a motivator for many of the ever growing number of searches for non-gravitational signals of dark matter. The experiments contributing to these efforts include direct detection experiments buried deep underground, searches for indirect astrophysical signals from dark matter annihilations, and even collider experiments, which may produce dark matter particles in their routine operations or detect its presence through precision tests of the Standard Model. While these searches have yet to detect any unambiguous signals of dark matter, they have placed very impressive constraints on dark matter parameter space.

As a popular theory for such an important phenomenon, it is only natural that there exist numerous variations on the WIMP paradigm. While the conventional WIMP possesses a mass somewhere in the range of tens of GeV to multiple TeV,

recent observations of a narrow, high-intensity 511 keV gamma-ray emission from the galactic center observed by the INTEGRAL satellite [7] has led to some interest in far lighter forms of dark matter, on the scale of a few MeV [8]. Such low mass dark matter, produced as a thermal relic and whose annihilations proceed through Standard Model states, would possess an annihilation cross section too small to generate a dark matter mass density compatible with that which is presently observed in the Universe. The dark matter simply freezes out too rapidly, and would therefore overclose the universe [9]. In order to bring the mass density of a weakly-interacting low mass dark matter scenario into agreement with empirical observations, new annihilation channels must be introduced. A convenient method of accomplishing this is to have the dark matter particles self-annihilate via states belonging to a hidden sector, uncharged under the Standard Model gauge group [10, 11, 12, 13, 14, 15]. Under such a scenario, it may even be possible that the 511 keV INTEGRAL line could be explained by the self-annihilation of MeV-scale dark matter into electron-positron pairs, as dark matter is widely expected to be present throughout the galactic bulge [8].

Of particular interest to the current work is a hidden sector dark matter scenario with a sub-GeV vector boson mediator and a scalar dark matter candidate. The p-wave suppression of the annihilation cross section greatly weakens constraints on the candidate's mass from cosmological and astrophysical observations. As a member of a hidden sector, its coupling to Standard Model states can be extremely weak, which largely spares the scenario from many of the constraints placed by collider experiments and precision tests of the Standard Model. Finally, its low mass renders it all but invisible to conventional direct dark matter detection experiments. Apart from possible, and highly model-dependent, indirect astrophysical signals from dark matter self-annihilations, it is rather difficult to probe this scenario by conventional methods of dark matter detection.

The question then naturally arises of whether some less conventional methods could be employed to effectively probe the parameter space of this hidden sector dark matter scenario. Direct dark matter detection experiments, often built deep underground to reduce their Standard Model background, attempt to do so by recording the recoils of nucleons from nucleon-dark matter scattering events. The low sensitivity of direct detection experiments to low mass dark matter is not due to the weak interaction strength of the dark matter with the Standard Model (though this does play a part), but rather because slow moving, low mass dark matter induces nuclear recoils too small to be detected by current generation experiments. However, the

scattering interactions between dark matter and nucleons suggest the possibility of its production through nucleon-nucleon collisions in collider experiments, where the dark matter would then be boosted to very large speeds. It was previously suggested by Batell, Ritz and Pospelov [16] that high-luminosity fixed target neutrino experiments could produce high intensity dark matter beams whose presence would then be detectable through additional neutral-current elastic scattering events in neutrino detectors (For work on similar searches, see e.g. [17, 18, 19, 20, 21, 22, 23, 24, 25]). A preliminary analysis was performed utilising data from the LSND experiment, and this dissertation will be concerned with confirming and expanding the previously reported results.

Our immediate objective is to determine the sensitivity of fixed target neutrino experiments to a hidden sector scenario possessing MeV-scale dark matter. We make use of two fixed target neutrino experiments in our analysis, LSND and MiniBooNE, both of which have published elastic scattering analyses with which to compare our own results. We wrote a Monte Carlo simulation of dark matter production resulting from the decays of neutral mesons produced at each of the experiments, and used it to determine the number of elastic scattering events each experiment would expect to observe under the dark matter scenario in question. The results of these simulations allow us to rule out large portions of the parameter space for dark matter with masses of a few MeV over a wide range of mediator masses, successfully probing parameter space that is largely inaccessible to direct dark matter detection experiments. The LSND and MiniBooNE experiments were still able to probe the scenario parameter space when the dark matter mass was increased, but their sensitivity suffered. Finally, we were also able to rule out this scenario as a candidate for producing the 511 KeV INTEGRAL line for the case where the mediator mass is at least twice the dark matter candidate's mass.

This work will be divided into five chapters, including this rather short introduction. We now offer a brief summary of what the reader can expect to find in each chapter:

Chapter 2 provides a survey of the numerous sources of gravitational evidence for the existence of dark matter, and an overview of the experiments that are attempting to detect it by non-gravitational means. A description of dark matter production in the thermal relic WIMP scenario will provide much of the dark matter background necessary. Finally, we embark on an in-depth discussion of the hidden sector dark matter scenario mentioned above, along with a much

more thorough motivation for choosing fixed target neutrino experiments as the most sensitive probes of the scenario.

Chapter 3 lays out the chain of processes by which a dark matter beam could be produced in one of these experiments and provides a brief description of the MiniBooNE and LSND experiments. A careful discussion of the simulation of the dark matter beam and its interactions with the neutrino detectors, and the method by which the simulation results are used to calculate the number of dark matter events round out the rest of the chapter.

Chapter 4 presents the results of the dark matter beam simulations with plots of the expected number of events for each experiment over the model parameter space, as well as some discussion and interpretation of these results.

Chapter 5 brings the dissertation to a close with a summary of the results and the work performed, as well as some discussion of future work.

Chapter 2

A Short Review of Dark Matter

There is an overwhelming amount of evidence indicating that baryonic matter is not the sole, nor even the primary, source of gravitational potential in the universe. We refer to this substance as dark matter, a placeholder term that encompasses a large number of possible explanations for a rather mysterious phenomenon. We can observe the effects of non-baryonic dark matter on a wide range of length scales and at a number of different times throughout the evolution of the universe. As elusive as dark matter has proven to be, we are not completely ignorant of its characteristics and properties. It appears to be far more abundant than baryonic matter, as baryons make up a mere 4% of the Universe's energy density, while 23% comes from dark matter. It interacts very weakly, if at all, with regular baryonic matter, as we have thus far been unable to observe it in any way other than through its gravitational effect on the less common but far more visible baryonic matter. Finally, it appears to have been cold, or non-relativistic, since the early universe. Present day dark matter is estimated to have an average velocity in the vicinity of the earth on the order of 200 km s^{-1} [26].

Before we can continue, we must introduce a bit of notation which will simplify the discussions for the rest of the chapter. Frequently, the abundance of some substance i in the universe is defined as

$$\Omega_i \equiv \frac{\rho_i}{\rho_c}, \tag{2.1}$$

where ρ_i is the energy density of i and ρ_c is the critical density of the universe, defined as

$$\rho_c \equiv \frac{3H^2}{8\pi G} \tag{2.2}$$

where H is the Hubble constant, and G is Newton's Constant. The critical density

is simply the average energy density required for the universe to be flat, a condition which we will not elaborate upon further here. We will denote the dark matter abundance by Ω_χ, the baryon abundance by Ω_b, and the matter abundance by Ω_M. Note that abundances are often quoted as $\Omega_i h^2$, where $h = H_0/100$ km s^{-1}Mpc$^{-1} \approx 0.719$ and $H_0 \approx 73$ km s^{-1} Mpc^{-1} is the present day value of the Hubble parameter [27].

The remainder of this chapter will be divided into four sections. We will begin with a somewhat brief survey of the evidence for dark matter in section 2.1 in order to motivate our interest in the topic. We will move on to a discussion of a possible production mechanism for dark matter in the early universe and the paradigm of the weakly interacting massive particle (WIMP) in section 2.2, and methods of searching for non-gravitational signals of dark matter in section 2.3. We will end with a description of a possible dark matter scenario in section 2.4. I am indebted to the authors of three written works that greatly aided me in writing this chapter, and would like to take a moment to mention each them here. Firstly, the TASI 2008 Dark Matter lecture notes by Hooper were an invaluable aid for their simple and concise explanations of dark matter related concepts [28]. The particle dark matter review by Bertone, Hooper and Silk provided a plethora of references for further reading and a very broad survey of the evidence for dark matter and non-gravitational searches [27]. Finally, the Bertone-edited reference text *Particle Dark Matter: Observations, Models and Searches* was an excellent complement to other sources, providing very in depth discussions on a number dark matter related topics [29].

2.1 The Evidence for Dark Matter

As mentioned previously, there is a great deal of evidence from a wide variety of sources for the existence of dark matter. Much of the enduring popularity of the dark matter hypothesis is due to its ability to explain a wide range of otherwise puzzling phenomena. Its ability to tie together numerous, disparate pieces of evidence on multiple length scales has allowed it to survive as a scientific hypothesis despite our current inability to directly detect it or to create it in collider experiments. We will begin with the evidence for dark matter on the scale of galaxies, and move to progressively larger length scales from there.

It is on the galactic scale that we find one of the most direct and easily grasped dark matter signals: the rotation curves of galaxies. A rotation curve is a plot of the

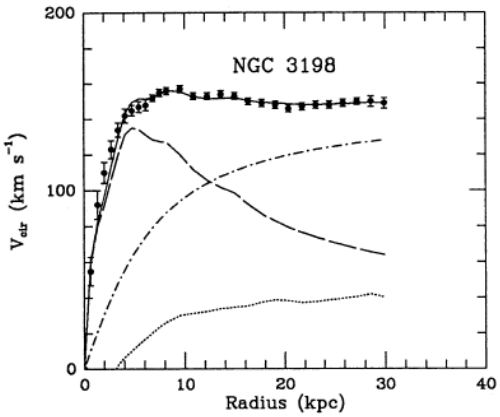

Figure 2.1: An example of a flat galactic rotation curve with the rotation curves of individual disk components included. The dashed curves correspond to visible components, the dotted to gas, and the dash-dotted curve to the dark matter halo [1]. Copyright © 1991 RAS.

rotational velocity of matter as a function of its distance from the galactic center. From Newtonian mechanics, we can calculate the rotational speed [27],

$$v(r) = \sqrt{\frac{GM(r)}{r}}, \tag{2.3}$$

where $M(r) = 4\pi \int dr' r'^2 \rho(r')$ and $\rho(r)$ is the mass density profile. From observations of gas and luminous matter in galaxies, it was expected that $\rho(r)$ would decrease as $1/\sqrt{r}$ outside of the luminous disk of the galaxy, and so we should see $v \propto \frac{1}{\sqrt{r}}$ as r increases. This was not observed in practice. Instead, we find that at large r, the evolution of v with distance levels off to a flat line (see Fig. 2.1), as if the visible matter were embedded in a much larger halo of unseen dark matter. The value of $M(r)$ would have to increase at a rate proportional to r to attain this evolution of $v(r)$. While $v(r)$ must eventually decrease for some large value of r if the mass of galaxy haloes are to remain finite, measurements of velocities out to even the largest distances have yet to detect this behavior. While other possible explanations for this phenomenon exist, dark matter is one of the simplest and most widely accepted. These rotation curves can be used to place a lower bound on the dark matter abundance in the universe of $\Omega_\chi \geq 0.1$ [30]. For illustrative plots of observed rotation curves, see e.g. [1] or [31].

There are a number of other galaxy-scale phenomena which can also be attributed to the influence of dark matter. Examples include the weak gravitational lensing of distant objects by unobserved foreground structures [32], the velocity dispersions of

the dark matter dominated dwarf spheroidals [33], and the velocity dispersions of spiral galaxy satellites [34].

If we move on to the scale of galaxy clusters, we find signs of dark matter in the motions of members of galaxy clusters in relation to one another. Fritz Zwicky was actually one of the first astronomers to suggest the dark matter hypothesis when in 1933 he applied the virial theorem to the Coma Cluster [35]. This is not to suggest that his was the first advancement of a dark matter-like hypothesis, as invisible objects had been suggested in the past as possible explanations for anomalous physical phenomena. Unexplained behaviour in the orbit of Uranus actually led to predictions of the existence of Neptune by Verrier and Adams in the 19th Century [27]. The virial theorem simply states that if we have some stable system of interacting particles, the average kinetic energy is equal to half the average potential energy,

$$\langle T \rangle = -\frac{1}{2}\langle V \rangle. \tag{2.4}$$

Zwicky discovered that the average gravitational potential energy calculated for the luminous matter in cluster was far smaller than the average kinetic energy of the luminous objects in the cluster. He estimated that the amount of mass in the cluster had to be at least two orders of magnitude higher than that calculated from adding up all of the luminous matter. This is, of course, quite a bit higher than what we would expect from other estimates of the relative dark matter and baryon abundances. However, with improved estimates of the amount of baryonic matter in a cluster, matter density estimates from the dynamics of galaxy clusters moves into agreement with other dark matter density estimates. Recent studies of galaxy cluster dynamics have been used to estimate the matter density of the universe, and find $\Omega_{\mathrm{M}} = 0.2 - 0.3$ (See e.g. [36] or [37]).

Also on the scale of galaxy clusters, we find an example of a spectacular event that happens to make one of the most compelling arguments for the existence of dark matter. Two galaxies clusters recently (at least on a cosmological scale) passed through one another in a system now called the Bullet Cluster. The baryonic gas in the clusters was rapidly decelerated through self-interactions and collisions. Gravitational lensing, however, reveals that the gravitational potential of the clusters has continued moving along ballistic trajectories while leaving much of the visible baryonic matter behind. It would appear that the dark matter halos of the two clusters passed through one another without decelerating due to their very weak self-interactions [38].

Some of the best estimates of the matter densities, for both dark and baryonic varieties, come indirectly from cosmological observations. A particularly interesting approach to estimating the matter densities present in the universe makes use of the background radiation from the last scattering, the point in time when the Universe had cooled sufficiently for photons to propagate freely. This background radiation is commonly known as the Cosmic Microwave Background (CMB). While the CMB is largely uniform, there are very slight temperature anisotropies that can be measured with experiments like the Wilkinson Microwave Anisotropy Probe (WMAP). These temperature fluctuations can be expanded as spherical harmonics and turned into a power spectrum. By comparing the relative heights of different peak in the spectrum, we can estimate matter densities. Using WMAP data, it was found that $\Omega_{\mathrm{b}}h^2 = 0.0227 \pm 0.0006$ and $\Omega_{\mathrm{M}}h^2 = 0.110 \pm 0.0006$ [30] (Numbers from PDG are based on [39] and [40]).

One can supplement the WMAP results with those from other cosmological sources. Big Bang Nucleosynthesis is used to predict the formation and abundances of the light elements such as Deuterium, Helium-3, Helium-4 and Lithium-7 in the early Universe. While we cannot use the light element abundances to directly probe the matter density though BBN, the only input to the process is the ratio of baryons to photons, and so it can be used to place constraints on the baryon density of the universe [41]. In addition, BBN places constraints on dark matter model building, as dark matter of sufficiently low mass ($m_\chi < 10$ MeV) to still be in chemical equillibrium during or after BBN will affect the abundances of the light elements [42]. It is important to stress that WMAP and BBN both place limits on the abundance of baryonic matter in the universe, while WMAP also indicates that the abundance of matter is much higher, which implies that dark matter is a non-baryonic form of matter.

The Sloan Digital Sky Survey (SDSS) is an effort to map the night sky, capturing images of millions of individual objects and hundreds of thousands of galaxies. The recorded power spectra of these galaxies can be used to independently calculate cosmological parameters. When combined with the WMAP results, these measurements can allow the relaxation of some assumptions made in WMAP-based calculations and the reduction of error bars in the calculation of Ω_{b} and Ω_{M} [43].

2.2 The Production of Dark Matter

One of the most common starting points for a dark matter theory is the paradigm of the Weakly Interacting Massive Particle, or WIMP. We will be using the WIMP as our starting point in our discussion of dark matter production in the early Universe. One of the simplest mechanisms for generating a dark matter abundance on the level seen in the current Universe is that of the Thermal WIMP or Thermal Relic. In this scenario, the WIMP abundance seen today is actually a relic left over from the much hotter early universe. Our discussion primarily follows the explanation provided by the 2008 TASI lecture notes on dark matter [28].

We will begin by positing the existence of a stable state χ, which will serve as our dark matter candidate. In the early universe, χ could be produced through processes involving Standard Model particles Y, $\chi\bar{\chi} \leftrightarrow Y\bar{Y}$. Alternatively, should our dark matter candidate be a Majorana particle, it would be $\chi\chi \leftrightarrow Y\bar{Y}$. In the early universe, when the temperature $T \gg m_\chi$, where m_χ is the mass of χ, the production and annihilation processes will be equally efficient, and χ will be present in large abundances alongside the more familliar Standard Model particles. As the temperature decreases, the χ production processes will be increasingly suppressed, while annihilation will proceed at a rate proportional to the square of the number density of χ, n_χ. So long as χ remains in thermal equilibrium, it will constantly approach its equilibrium number density. In the nonrelativistic regime, where $T \lesssim m_\chi$, we can write this as

$$n_{\chi,\mathrm{eq}} = g_\chi \left(\frac{m_\chi T}{2\pi}\right)^{3/2} e^{-m_\chi/T}, \tag{2.5}$$

where g_χ is the number of internal degrees of freedom for our dark matter particle.

Should χ remain in chemical equilibrium indefinitely, its number density will continue to be depleted with decreasing temperature until it no longer makes up a cosmologically significant fraction of the energy density of the Universe. As we have good reason to believe that dark matter actually makes up a dominant portion of the matter density of the universe, some mechanism must be found to suppress the annihilation rate in order for our candidate to continue playing an important role in the evolution of the Universe. We quickly see that Hubble expansion naturally fulfills this requirement by looking at the Boltzmann equation governing the number density

of χ,

$$\frac{dn_\chi}{dt} + 3Hn_\chi = -\langle\sigma_{\chi\bar{\chi}}v\rangle\left(n_\chi^2 - n_{\chi,\mathrm{eq}}^2\right), \tag{2.6}$$

where H is the Hubble parameter representing the expansion rate of the Universe. It can be written as,

$$H = \sqrt{\frac{8\pi^3\rho}{3M_{\mathrm{Pl}}}}, \tag{2.7}$$

where M_{Pl} is the Planck Mass, ρ is the energy density of the universe and $\langle\sigma_{\chi\bar{\chi}}v\rangle$ is χ's self-annihilation cross-section multiplied by the relative speed between two dark matter particles v, thermally averaged over the velocity of χ particles. The velocity distribution is normally taken to be a Maxwell-Boltzmann distribution centered on some average speed $\langle v\rangle$. For $T \gg m_\chi$, the terms on the right hand side of the equation dominate, and n_χ naturally tends to its equilibrium value, $n_{\chi,\mathrm{eq}}$. Once T drops such that $T \ll m_\chi$, $n_{\chi,\mathrm{eq}}$ becomes very small, leaving $3Hn_\chi$ and the annihilation term on the right hand side to further decrease n_χ. Afterwards, n_χ continues to decline until it becomes small enough that the factor of n_χ^2 suppresses the annihilation term to the point of insignificance, the dark matter drops out of chemical equillibrium and the Hubble expansion term dominates. The point where dark matter particles cease to annihilate at an appreciable rate is called freeze-out. The larger the annihilation rate, the later freeze-out occurs and the lower the relic density becomes. The temperature at which freeze-out occurs, T_{FO}, is determined by numerically solving the Boltzmann equation. To do this, we approximate the thermally averaged cross-section for non-relativistic speeds as

$$\langle\sigma_{\chi\bar{\chi}}v\rangle = a + b\langle v^2\rangle + \mathcal{O}(v^4), \tag{2.8}$$

and define a new variable $x \equiv m_\chi/T$. We then determine the freeze-out solution by iteratively solving the following equation,

$$x_{\mathrm{FO}} = \frac{m_\chi}{T_{\mathrm{FO}}} \approx \ln\left(c(c+2)\sqrt{\frac{45}{8}}\frac{g_*}{2\pi^3}\frac{m_\chi M_{\mathrm{PL}}(a+6b/x_{\mathrm{FO}})}{g_*^{1/2}x_{\mathrm{FO}}^{1/2}}\right), \tag{2.9}$$

where c has been numerically determined to be ~ 0.5, and g_* is the total number of relativistic degrees of freedom in the Standard Model. It decreases with falling temperature, as heavy species become nonrelativistic. One can then find an approximate

expression for the WIMP density in the present day Universe,

$$\Omega_\chi h^2 \approx \frac{1.04 \times 10^9 \mathrm{GeV}^{-1}}{M_{\mathrm{PL}}} \frac{x_{\mathrm{FO}}}{g_*^{1/2}(a + 3b/x_{\mathrm{FO}})}. \tag{2.10}$$

Note that the higher the annihilation rate, the later freeze-out occurs and the lower the WIMP relic density becomes. For masses on the order of a few GeV to a TeV, freeze out occurs somewhere in the range of $x_{\mathrm{FO}} = 20$ to 30, and one can approximate (2.10) as [27],

$$\Omega_\chi h^2 \approx \frac{3 \times 10^{-27} \mathrm{cm}^3 s^{-1}}{\langle \sigma_{\chi\bar{\chi}} v \rangle}. \tag{2.11}$$

This equation embodies what is sometimes referred to as the WIMP miracle. When we calculate the relic density for a dark matter particle with a weak scale mass ($m_\chi \sim 100$ GeV $-$ 1 TeV) and a weak scale scattering cross-section, one reproduces the dark matter density of the present day Universe. This extremely suggestive result is perhaps a coincidence, but it has certainly helped provide some popularity to the WIMP paradigm.

We have now examined one of the simplest production processes for dark matter, and in the WIMP Miracle, one of the reasons for the enduring popularity of the WIMP paradigm. This is, of course, not the only way in which the present day dark matter density can be produced (there are a number of variations on just the thermal relic scenario alone), but it is sufficient background for a discussion of the dark matter scenario that will be examined in section 2.4. We will now move on to survey some of the many ways in which modern experiments are searching for dark matter.

2.3 Searching for Dark Matter

In section 2.1, we laid out a wide array of observational evidence for the existence of dark matter, but all of the signals of dark matter describe there were observed purely through dark matter's gravitational interactions with the visible baryonic matter. While these efforts have been invaluable sources of information on dark matter, in order to learn more about the characteristics of individual dark matter particles and its mechanism(s) for interacting with the Standard Model, we need to collect non-gravitational evidence for its existence. A plethora of efforts employing a range of very different search strategies are under way in pursuit of this goal, and we will attempt to give an overview of some of the most popular search strategies in this

section.

2.3.1 Direct

We begin with one of the most conceptually straightforward strategies, direct detection. A direct detection experiment seeks to observe the interactions between the nuclei that compose a detector and dark matter particles belonging to the ambient dark matter density that our gravitational observations have indicated should constantly be passing through the Earth. Direct detection experiments are capable of constraining the parameter spaces of a wide variety of dark matter scenarios by providing very stringent limits on the nucleon-WIMP scattering cross-sections for a wide range of dark matter masses. However, their sensitivity drops sharply when dark matter possesses either a very small or very large mass. For small masses, this is because the recoil energy of the nucleon,

$$E_{\text{recoil}} = \frac{m_\chi^2 M_{\text{nucleus}} v^2 (1 - \cos\theta)}{(m_\chi + M_{\text{nucleus}}^2)}, \tag{2.12}$$

where θ is the angle of the dark matter particle after scattering, can be heavily suppressed by a small dark matter to nucleon mass ratio, making detection of scattering events more difficult or impossible depending on the experiment [28]. Very massive dark matter has its scattering rate suppressed by the dark matter flux,

$$\Phi_\chi \propto \frac{1}{m_\chi}, \tag{2.13}$$

which declines with increasing m_χ. This is wonderfully illustrated in Fig. 2.2.

Direct detection experiments seek to determine the rate at which dark matter particles interact with their detectors (if at all), and the spectrum of energies with which they scatter. Challenges arise in the suppression of the interaction rate by the possibly very small WIMP nucleon scattering cross-section, and depending on the WIMP mass, the difficulty of detecting these events due to very small nuclear recoils. In addition, these experiments must contend with background from the interactions of Standard Model particles passing through the detector, and are normally conducted deep underground so as to be shielded from cosmic rays.

There are a number of different techniques used in direct detection, a diversity that is quite useful for controlling uncertainties. As an example, experiments can

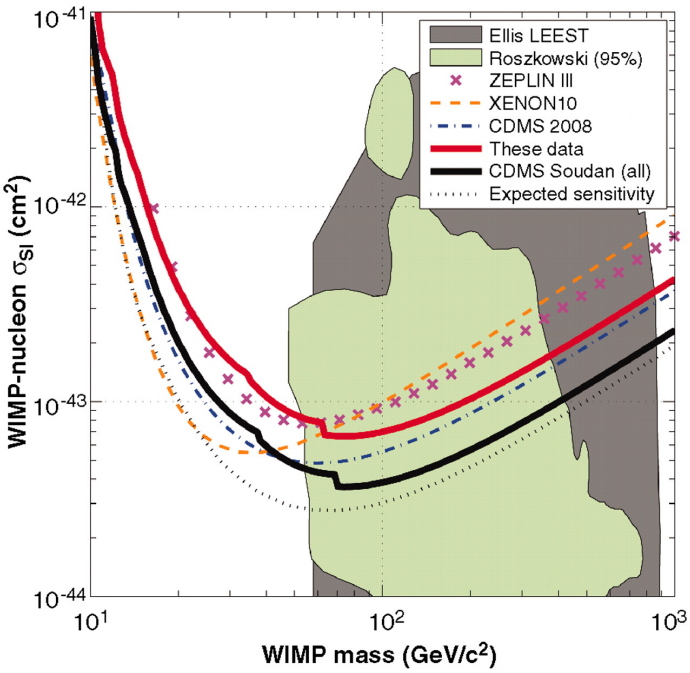

Figure 2.2: Sensitivity of a number of leading direct detection experiment produced by the CDMS collaboration [2]. Note the slowly decreasing sensitivity as the mass increases, and the sharp decline in sensitivity as the dark matter mass approaches 10 GeV. We should note here that updated sensitivity plots have been produced by XENON100, and are currently awaiting publication [3]. Copyright © 2009 Science.

study Spin-Dependent (SD) or Spin-Independent (SI) scattering [27]. SD scattering studies the axial-vector couplings to nucleon spins, and the interaction cross-section is proportional to the angular momentum of the nucleon, $J(J+1)$. SI scattering probes scalar and vector couplings, and scales with the number of nucleons in the nucleus. As direct detection experiments can utilize very large nuclei, SI scattering tends to provide far greater sensitivity than SD scattering. However, this is not to suggest that SD scattering does not have a place in dark matter searches, as should dark matter couple to regular matter solely through the axial-vector current, it would not be detectable through SI scattering at all. Currently, the best limits on the SI WIMP-nucleon scattering cross-section are provided by experiments like CDMS [2] and XENON [3], while COUPP [44], KIMS [45] and PICASSO [46] provide the best limits for SD scattering.

Another choice to make is whether to study elastic or inelastic scattering [27]. Elastic scattering is fairly obvious, the dark matter interacts with the nucleus as a whole and the experiment attempts to measure the energy of the recoiling nucleus.

Current day experiments can detect recoils as low as a few keV. Inelastic scattering involves the excitation of electrons orbiting the nucleus, which emit a photon shortly afterwards. Experiments then have to detect the photon while screening out background from ambient radiation. As a final note, some direct detection experiments seek to observe a modulation in the dark matter signal as the Earth orbits around the Sun. The most well known of these is likely the DAMA/LIBRA experiment, which has long claimed to have observed this dark matter modulation, though it is difficult to accomodate their signal with the null results of other direct detection experiments [47].

2.3.2 Indirect

Indirect detection experiments seek to use telescopes to observe the products of dark matter self-annhilation events, which could include gamma-rays, positrons, electrons, antiprotons and neutrinos. The most promising locations to look for these products feature regions that are expected to have particularly high dark matter densities, as the annihilation rate is proportional to the number density squared (as seen in equation (2.6)). We will focus on gamma-rays, as they are of particular interest to the dark matter scenario described in section 2.4, with a brief discussion of some of the other cosmic particles which could hint at dark matter annihilation processes afterwards.

Gamma-rays have a few advantages in the indirect study of dark matter. They are not attenuated over galactic distance scales, thus retaining their spectral information, nor are they deflected by magnetic fields, allowing gamma-rays to also provide information about the angular distribution of its source. The energy spectrum is heavily dependent on the type of dark matter, specifically which Standard Model particles tend to be pair produced in annihilation events. The photons could also be produced directly from the dark matter self-annihilations themselves, rather than after an intermediate step through a Standard Model state.

The galactic center is an especially promising region to search for gamma-rays produced from dark matter annihilations due to its expected high concentration of dark matter [48]. However, there are complications inherent in searching for dark matter in the galactic core [28]. It is actually very difficult to determine the dark matter density profile in the galactic center as N-body simulations, one of the conventional methods used to determine the large scale distribution of dark matter in the

universe, do not have sufficient resolution to resolve the galactic center. Complicating attempts at dark matter simulation even further, the galactic center is one of the few regions whose gravitational potential is dominated by baryonic matter, which is not accounted for by dark matter simulations. Finally, there may simply be too much background in the galactic center to disentangle a dark matter signal. Should the dark matter signal in the galactic center be washed out by baryonic backgrounds, it may be profitable to look to other areas of the sky, such as nearby dwarf spheroidals [49, 50] or in the dark matter halo surrounding our galaxy [51] for gamma-ray signals of dark matter.

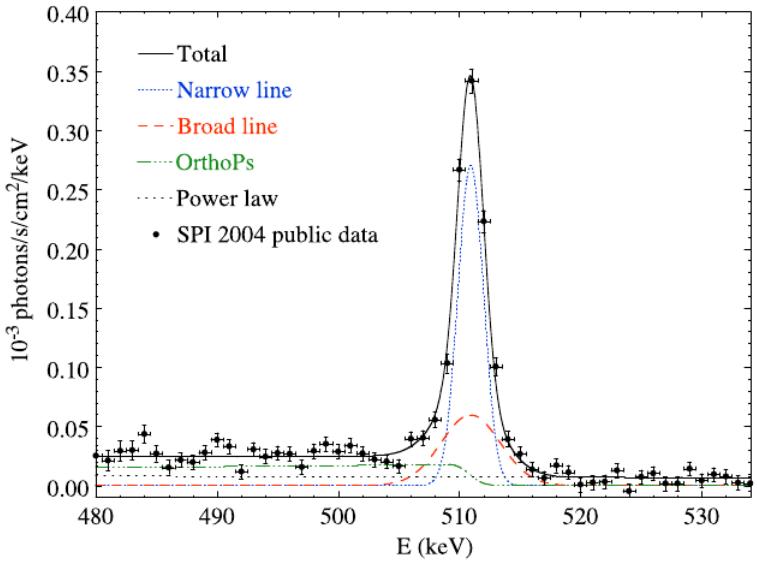

Figure 2.3: Fit of the spectrum measured by the SPI gamma-ray spectrometer aboard the INTEGRAL satellite. The dashed and dotted lines correspond to the broad and narrow peak components, respectively [4]. Copyright © 2006 ESO.

Even considering these difficulties, there has been an observed candidate for a dark matter signal from the galactic center in the form of the 511 keV gamma-ray line first observed in the 1970's and more recently measured by the INTEGRAL satellite [7]. The INTEGRAL line appears as a narrow peak in the gamma-ray spectrum recorded from the center of the galaxy, though it is actually best described as the superposition of a narrow and broad peak component. The narrow component (FWHM=1.3 ± 0.4 keV) is consistent with annihilations of electrons and positrons that are nearly at rest, while the broad component (FWHM=5.4 ± 1.2 keV) matches the broadening expected from the annihilation of positronium through charge exchange with hydrogren (see

Fig. 2.3).

The INTEGRAL line would require the production of 3×10^{42} positrons per second [8] in the galactic bulge, which is quite a bit higher than was expected from conventional cosmic sources, though ideas as to how it could be produced in more exotic stellar events, such as hypernovae or gamma-ray bursts [52], have been advanced. Adding to the complications of explaining the 511 keV line is that it appears to be distributed throughout the galactic bulge (though with a discernable disk component, as has recently been reported by INTEGRAL [53]), so not only do we need to find new positron sources, but we also need a means by which these positrons could be propagated throughout the galactic bulge. Low mass dark matter with a mass in the range of a few MeV has been advanced as one possible source for the 511 keV line as it is distributed throughout the galactic bulge and could easily decay into positron-electron pairs. It should be stressed that the dark matter must have a low mass, no larger than a few MeV, in order to reproduce the observed spectrum of the 511 keV INTEGRAL line. Should the dark matter be too heavy, the positrons would be injected into the galactic medium at relativistic speeds, leading to the production of higher energy gamma-rays in addition to those observed from the 511 keV line [54]. We will discuss a possible dark matter scenario with the potential to produce this phenomenon in section 2.4.

The only method of directly detecting gamma-rays is to use satellite-based telescopes such as FERMI (formerly known as GLAST) or INTEGRAL as photons with energies on the order of magnitude of cosmic gamma-rays are incapable of penetrating the atmosphere. This does not mean we are completely unable to study gamma-rays from the ground. The entry of highly energetic photons into the atmosphere triggers a cosmic air shower that can be detected by ground based atmospheric Cherenkov detectors such as HESS, MAGIC and VERITAS. The two observational methods are quite complementary [27], as satellite based telescopes like Fermi are capable of observing a large portion of the sky, but their size and effective area are necessarily limited by their need to be boosted into orbit. Ground based telescopes can be built with far larger effective areas, but can only observe a much smaller portion of the sky.

Neutrinos provide another promising means of detecting dark matter, and share with gamma-rays the advantage of not being deflected by galactic magnetic fields. They are difficult to detect due to their weak interaction strength, though this also allows neutrino experiments to be constructed deep underground where they can be shielded from background. The sun could provide a local source of neutrinos

produced in dark matter annihilations through solar trapping. Dark matter particles could be trapped in the center of the sun where they could then self-annihilate, producing neutrinos which could easily escape the sun and propagate to earth-bound detectors [28]. Positrons and anti-protons could also serve as signals of dark matter, though likely only very indirectly. As they are charged particles, their trajectories are heavily influenced by galactic magnetic fields, and they do not allow us to extract angular information that indicate their sources. Still, excesses in their production (such as those reported by PAMELA [55]) could point to the presence of dark matter annihilations in the galaxy.

2.3.3 Collider

A third strategy for dark matter searches is to study them with particle colliders, where we can attempt to either produce dark matter states during regular collider operation, or place limits on dark matter models by performing very high precision measurements of Standard Model interactions sensitive to the existence of dark matter states. A collider experiment would likely only notice the production of dark matter through missing energy in a collision, where some particle was created and propagated out of the detector without being detected. This particle would necessarily have to be long-lived, as otherwise it could decay inside of the detection apparatus and be identified through its decay products, and weakly-interacting. There are sources of missing energy already extent in the Standard Model (neutrinos being a prime example), and the effects of a dark matter candidate would have to be disentangled from these conventional signals. This is all highly dependent on the dark matter model being studied, of course. Of some interest to this thesis, and an example of a missing energy signal, is the invisible width of the Z-boson. If a dark matter candidate is sufficiently light, it may be produced in decays of Z bosons, $Z \to \chi\bar{\chi}$. The LEP2 experiment has placed constraints on this width, placing the limit $\Gamma_{Z\to\chi\bar{\chi}} < 4.2$ MeV [27]. Colliders have also imposed constraints on the masses of new charged particles, new gauge bosons, flavour changing neutral currents, rare B decays, and high precision measurements of the magnetic moment of the muon place further constraints on the coupling between light dark matter and Standard Model states. In addition, the Large Hadron Collider recently began operations, and is set to probe substantial portions of the parameter space of many dark matter models.

2.4 The Hidden Sector Dark Matter Scenario

The Lee-Weinberg limit places a lower bound of a few GeV on the masses of dark matter candidates, as dark matter with a mass below this limit would be overproduced, and would therefore overclose the universe [9]. However, this limit is not ironclad, as some assumptions were made in performing this calculation. The original paper was studying a heavy neutrino, and assumed that the self-annihilation proceeded through Standard Model states, but this need not necessarily be the case. The constraints on the mass scales available to a thermal relic WIMP are greatly weakened if the WIMP's self-annihilation is mediated by some hidden sector state, uncharged under the Standard Model gauge group [56]. Positing the existence of hidden sector states is not particularly exotic, as there already exist matter fields in the Standard Model uncharged under one or more gauge groups, and hidden sectors are a common component of new physics scenarios. Dark matter possessing a mass of a few MeV to a few GeV is of particular interest, as the sensitivity of direct dark matter detection experiments is drastically weakened in this mass regime. Dark matter with a mass of a few MeV may even be able to explain the 511 keV INTEGRAL line (see section 2.3.2), and we will use this intriguing possibility as motivation for some of our model building choices while assembling a low mass dark matter scenario.

The interactions of some hidden sector, uncharged under Standard Model gauge group, with Standard Model states can be parameterized as [16]

$$\mathcal{L}_{\text{mediation}} = \sum_{k,l,n}^{k+l=n+4} \frac{\mathcal{O}_{\text{NP}}^{(k)} \mathcal{O}_{\text{SM}}^{(l)}}{\Lambda^n}, \tag{2.14}$$

where $\mathcal{O}$ are New Physics (NP) and Standard Model (SM) operators of dimension k and l, and Λ is some very large cut off scale. The case of the greatest importance for this work is that of marginal $n = 0$ interactions. The SM operators of lowest dimension are collectively known as portals [57, 58, 59, 60, 61], and include

$$\begin{array}{ll} F_{\mu\nu}^{Y} & \text{Vector Portal} \\ H^{\dagger}H & \text{Higgs Portal} \\ LH & \text{Neutrino Portal} \end{array}, \tag{2.15}$$

where $F_{\mu\nu}^{Y}$ is the hypercharge field strength, and H and L are the Higgs and Lepton doublets, respectively. These operators can be used to couple the SM to new physics

without making assumptions about the mass scale of the new physics fields, and are unsuppressed by any heavy scale. The Higgs and Neutrino portals are unsuitable for a low mass dark matter scenario for phenomenological reasons. Specifically, the Higgs portal is rendered problematic by measurements of Kaon decays (amongst others), while the direct coupling to neutrinos leads to unacceptable distortions of observed supernova spectra through the suppression of neutrino energies for dark matter with a mass of a few MeV (See e.g. [62]). We will choose to couple our dark matter scenario through the Vector portal, as it does not fall prey to these difficulties.

We require that the interaction term linking the Standard Model with this hidden sector be gauge invariant, and we charge the hidden sector under a U(1) gauge group. Following in the footsteps of previous work [10, 14], we have chosen to use a U(1)$'$ gauge boson, V, as a mediator with the following interaction term

$$\mathcal{L}_{\text{int}} = \frac{\kappa}{2} V_{\mu\nu} F_Y^{\mu\nu}, \tag{2.16}$$

where κ serves as a coupling constant, $V_{\mu\nu}$ and $F_Y^{\mu\nu}$ are the U(1)$'$ and hypercharge field strengths, respectively. Note that while the V mixes with the hypercharge boson, interactions between the Z and V will be too weak (due to suppression by the mass of the Z) to have any effect on the analysis, and so we will only consider the coupling to the photon through $F^{\mu\nu}$. The coupling constant κ can be rescaled accordingly after electroweak symmetry breaking. The scenario does couple the dark matter candidate to neutrinos, but as it is through the Z, it can be safely ignored for the reasons mentioned previously.

We can now consider the model itself. Before symmetry breaking, the Lagrangian takes the form

$$\mathcal{L}_{V,\chi} = -\frac{1}{4} V_{\mu\nu}^2 - \frac{\kappa}{2} V_{\mu\nu} F^{\mu\nu} + |D_\mu \phi|^2 - U(\phi\phi^*) + |D_\mu \chi|^2 - m_\chi^2 |\chi|^2, \tag{2.17}$$

where χ is a scalar dark matter candidate with charge e' under the U(1)$'$ gauge group, m_χ is the mass of the χ, and the U(1)$'$ covariant derivative is defined as $D_\mu = \partial_\mu + ie'V_\mu$. The U(1)$'$ symmetry is spontaneously broken at low energies by a Higgs$'$, which provides a mass term for the U(1)$'$ gauge boson. The mediator interacts with Standard Model states through kinetic mixing with the vector portal, $F^{\mu\nu}$. After

symmetry breaking, the Lagrangian takes the form

$$\mathcal{L}_{V,\chi} = -\frac{1}{4}V_{\mu\nu}^2 + \frac{1}{2}m_V^2 V_\mu^2 + \kappa V_\nu \partial_\mu F^{\mu\nu} + |D_\mu \chi|^2 - m_\chi^2 |\chi|^2 + \mathcal{L}_{h'}, \tag{2.18}$$

where m_V is the mass of the V. All of the kinetic terms and interactions involving the Higgs$'$ are hidden away in $\mathcal{L}_{h'}$ and they will play no further role in our discussion or the analysis of this scenario. We do, however, impose the condition $m_{h'} > m_\chi$.

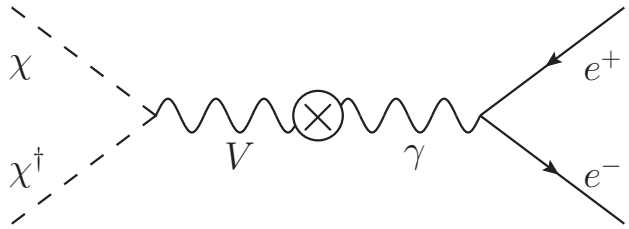

Figure 2.4: Tree-level self-annihilation diagram for scalar dark matter into electron-positron pairs. This is the dominant diagram for annihilation of dark matter into Standard Model states for the masses being considered.

Further analysis has determined that dark matter candidates with masses under 100 MeV are excluded by observations of astronomical gamma-rays if their annihilation cross-section possesses an s-wave component, so $\langle \sigma v \rangle = \text{ constant } + \mathcal{O}(v^2)$ [56]. The annihilation rate in the galactic center must be suppressed by several orders of magnitude relative to the rate at freeze-out. In terms of the cross-section parameterization of equation (2.8), we must find an annihilation mechanism for which $a = 0$, which translates to

$$\langle \sigma v \rangle = bv^2 + \mathcal{O}(v^4). \tag{2.19}$$

This can be satisfied so long as the mass of the Vector mediator is larger than that of the dark matter candidate, $m_V > m_\chi$, and the dark matter candidate is a scalar particle. In the case of $m_V < m_\chi$, the annihilation proceeds as an s-wave process, and the scenario is necessarily excluded.

The scenario posseses four real parameters: the strength of the mixing between the V mediator and the Standard Model photon, which we have labelled κ, the masses of the V mediator and χ dark matter candidates, and the charge of χ under the U(1)$'$ gauge group, labelled e' but normally encapsulated inside α'. We can place constraints upon the theory in order to reduce the number of free parameters, and we will do so by assuming that our dark matter candidate is the dominant contributor

to the dark matter density in the universe,

$$\frac{\Omega_{\rm DM}}{\Omega_\chi} \sim 1.$$

To impose this constraint, we will of course need to determine the dark matter density predicted by our scenario for a given set of model parameters. Looking back at the end of section 2.2, we see that the relic density at freeze-out is determined by the thermally averaged dark matter cross-section. For the dark matter masses we will be considering ($m_\chi \in [1, 100]$ MeV), the dominant annihilation process will be to an electron-positron pair (see Fig. 2.4) as the coupling to neutrinos is heavily suppressed by the Z mass and direct annihilation to photons is also suppressed [14]. The expression for the cross-section follows,

$$\langle\sigma v\rangle_{\rm ann} \sim 3\times10^{-27}\,{\rm cm}^2\times\left(\frac{\kappa^2\alpha'}{\alpha}\langle v^2\rangle\right)\times\left(\frac{\rm MeV}{m_\chi}\right)^2\times\sqrt{1-\frac{m_e^2}{m_\chi^2}}\left(\frac{4m_\chi^2}{4m_\chi^2-m_V^2}\right), \quad (2.20)$$

where $\langle v\rangle \sim 0.3$ at freeze-out, and we have dropped terms proportional to m_e^2 and made the approximation $E_\chi \approx m_\chi$. As mentioned in section 2.3.2, WMAP surveys of the CMB have allowed them to constrain the relic density to $\Omega_{\rm DM}h^2 \sim 0.1 \sim (0.1{\rm pbn})/\langle\sigma v\rangle_{\rm fo}$, where $\langle\sigma v\rangle_{\rm fo}$ is the thermally averaged cross-section at freeze-out. Combining the WMAP measurements with (2.20), we find the following expression,

$$\frac{\alpha'\kappa^2}{\alpha}\times\left(\frac{100\ {\rm MeV}^2}{4m_\chi^2-m_V^2}\right)^2\times\left(\frac{m_\chi}{1\ {\rm MeV}}\right)^2\times\sqrt{1-\frac{m_e^2}{m_\chi^2}} \sim 3\times10^{-6}. \quad (2.21)$$

In order for the hidden sector scenario to be a viable explanation for a substantial portion of the dark matter in the universe, it must satisfy (2.21). This constraint is easily satisfied by varying the four model parameters, and we can use this expression to rewrite one of the model parameters in terms of the others. It will become important to do so in section 3.1, and so we will leave this task for the next chapter.

It is possible that this dark matter scenario could explain the 511 keV line observed by INTEGRAL should m_χ be equal to a few MeV. In order to produce the observed flux of positrons, the following condition must be satisfied [14],

$$N_{e^+}\langle\sigma v\rangle_g\times\left(\frac{1\ {\rm MeV}}{m_\chi}\right)^2 \sim 10^{-40}{\rm cm}^2\times\frac{\Phi_{511,\chi}}{\Phi_{511,{\rm total}}}, \quad (2.22)$$

where $\Phi_{511,\chi}/\Phi_{511,\text{total}}$ is the fraction of the observed gamma-ray signal from the galactic center produced by the self annihilation of dark matter, N_{e^+} is the number of positrons produced in a dark matter self-annihilation event, and $\langle\sigma v\rangle_g$ is the annihilation cross-section thermally averaged over the velocity distribution expected for dark matter in the galactic center. In our case, the dominant decay process is $\chi\chi^\dagger \to e^+e^-$, and so N_{e^+}=1. The dark matter annihilation rate scales as n_χ^2 and as the dark matter density profile is very poorly known in the galactic center (as we noted in section 2.3.2), equation (2.22) is only accurate to within one or two orders of magnitude.

Equation (2.22) will automatically be satisfied (to our low working precision, at least) once we enforce the conditions from equation (2.21). While it would be very exciting if our scenario could produce the observed gamma-ray flux in the galactic center, so long as it does not produce a flux dramatically larger than that observed by INTEGRAL, we will not overly concern ourselves with equation (2.22), nor will we limit ourselves to dark matter masses capable of producing the observed flux during our later analysis of the scenario in Chapter 3. We will, of course, revisit the feasibility of explaining the INTEGRAL line with this dark matter scenario in the discussion of our results in Chapter 4.

This dark matter can, of course, interact with Standard Model particles and nuclei, and we should consider the constraints imposed by direct detection experiments. Disregarding the actual rate of scattering between our dark matter scenario and the nuclei used by direct detection experiments, the low recoil energies will provide the primary challenge for direct detection of low mass hidden sector dark matter. Looking back to equation (2.12), and taking $M_{\text{nucleus}} = 10$ GeV, $m_\chi \ll M_{\text{nucleus}}$, and $v \sim 0.001$, we can make a rough estimate of the recoil energies to be expected for low mass dark matter,

$$E_{\text{recoil}} \sim 10^{-4}\text{eV} \times \left(\frac{m_\chi}{1\text{ MeV}}\right)^2. \tag{2.23}$$

For $m_\chi \in [1, 100]$ MeV, this is far below the sensitivity of any current direct dark matter detection experiment, and as was mentioned in passing at the beginning of the section, direct detection experiments are largely insensitive to this dark matter scenario.

Were the dark matter boosted to a speed that was a significant fraction of c, it becomes possible that its scattering with Standard Model particles would become detectable. It is possible that the production of dark matter at high-luminosity fixed

target experiments could yield a detectable signal, with the large collision-number statistics serving to overcome the weakness of its interactions with Standard Model states. It is difficult to determine with any great certainty whether a fixed target experiment would be more sensitive than high-energy collider experiments, but there are a few simple arguments in their favour for the case of light hidden sector states [16]. The production cross-section for a marginal or irrelevant operators of dimension $4+n$ can be written as

$$\sigma \sim \frac{1}{E^2}\left(\frac{E}{\Lambda}\right)^{2n}, \tag{2.24}$$

where Λ is the large mass scale previously seen in (2.14). If we take the integrated luminosity of a collider experimen to be $\mathcal{L}_c \sim 10^{41}$ cm^{-2}, and the equivalent luminosity for a fixed target experiment with a 1 meter target and 10^{21} protons on target can be estimated to be $\mathcal{L}_t \sim 10^{21} \times 10^{24}$ cm$^{-3} \times 100$ cm, where we have taken the number density of the detector to be a small multiple of Avogadro's number $\sim 10^{24}$. We will take the center of mass energy of a collider to be the design energy of the LHC, $E_c = 14$ TeV, and that of a fixed target collider to be $E_t = \sqrt{2m_p E_{\rm lab}} \sim 1.4 \times 10^{-2}$ TeV for $E_{\rm lab} = 100$ GeV. For the $n = 0$ marginal interactions that we are most interested in, we find

$$\frac{N_{\rm collider}}{N_{\rm target}} \sim \frac{\mathcal{L}_c}{\mathcal{L}_t} \times \left(\frac{E_c}{E_t}\right)^{2n-2} \sim 10^{-12}. \tag{2.25}$$

Our naive estimate gives a clear and overwhelming advantage to fixed target experiments. In addition, fixed target neutrino experiments also tend to possess quite large detector volumes, further aiding efforts at dark matter detection, though the geometric acceptance of the detectors may counteract this enhancement to the signal. It would appear that fixed target experiments provide our best chance for detecting a signal from low mass hidden sector dark matter, though particularly high luminosity collider experiments may also merit study.

Over the course of this chapter, we have laid out the observational case for dark matter, and the as of yet unsuccessful efforts to detect it by some means other than its gravitational interactions with the baryonic matter of the Universe. We described the most popular dark matter paradigm, the thermal WIMP, and building from there, developed a variant of the WIMP scenario in hidden sector dark matter whose interactions with the Standard Model are mediated by a sub-GeV vector mediator. This scenario was developed with the aim of simultaneously generating the observed

dark matter density in the Universe while explaining the 511 KeV line observed by the INTEGRAL satellite. We will investigate the possibility that this scenario could result in a detectable dark matter beam at fixed target neutrino experiments in the next two chapters.

Chapter 3

Fixed Target Probes

3.1 Dark Matter Beams at Fixed Target Experiments

Within the hidden sector scenario discussed previously in section 2.4, and for sufficiently small m_V, the following chain of processes can produce an energetic dark matter beam at a fixed target neutrino experiment:

1. $p + p \rightarrow X + \pi^0, \eta$
2. $\pi^0, \eta \rightarrow \gamma + V$
3. $V \rightarrow 2\chi$

As the π^0 and the η both have decay lengths on the order of a few nanometers ($c\tau_{\pi^0} = 25.1$nm, $c\tau_\eta \simeq 0.2$nm), the first two steps steps of the chain take place within the target. The decay length of the V is dependent upon α', m_V and m_χ, but over the parameter space of concern to this analysis will always be short enough to ensure that it decays before exiting the target. The vast majority of the dark matter particles produced at a fixed target neutrino experiment in this scenario will be the products of decays in flight.

We have focused on these hadronic states primarily due to their large branching fraction to photons. Whether the decays of π^0's or η's serve as the dominant dark matter production mode is largely dependent on the mass of the V. While for most of $m_V < m_{\pi^0}$, the π^0 is by far the dominant production mechanism, the inclusion of the η production mode allows us to probe far larger m_V, and therefore larger m_χ,

though the η production mode's signal will be weaker due to its smaller production cross-section in nucleon-nucleon collisions relative to that of the π^0. This will be discussed further in section 3.3.2.

The baryonic state $\Delta(1232)$ was also considered as a possible source of a dark matter beam, as its decays are one of the primary sources of pions at fixed target neutrino experiments, and should therefore be produced at a comparable rate. Its branching ratio to a single photon, while small, is not so small as to render it insensitive to the hidden sector scenario. We chose not to pursue this avenue of inquiry primarily because the η decay mode can access a significantly larger range of V and χ masses than the $\Delta(1232)$.

For both π^0 and η, the branching ratio to a $V\gamma$ final state is proportional to that of the radiative decays of the mesons to two photons, though suppressed by a factor of κ^2 and phase space factors involving the ratio of m_V to m_ϕ where $\phi = \pi^0, \eta$,

$$\mathrm{Br}_{\phi\to V\gamma} \simeq 2\kappa^2 \left(1 - \frac{m_V^2}{m_\phi^2}\right) \mathrm{Br}_{\phi\to\gamma\gamma}. \tag{3.1}$$

For the case of π^0 decays, $\mathrm{Br}_{\pi^0\to\gamma\gamma} \simeq 1$, while for η decays, $\mathrm{Br}_{\eta\to\gamma\gamma} \simeq 0.39$.

As we require that $\kappa \ll 1$, and assuming $m_V > 2m_\chi$, we find that $\mathrm{Br}_{V\to\chi\chi} \simeq 1$, and the rapid decay of V's results in a dark matter beam that propagates alongside the neutrino beam to the detector. For the range of κ values we will consider in the following analysis, dark matter possesses a weak scale scattering cross-section with normal matter, and therefore could be detected through neutral current-like scattering processes. We will consider elastic scattering interactions with both electrons, $e+\chi \to e+\chi$, and nucleons, $N+\chi \to N+\chi$ (see Fig. 3.1). We will probe the scenario by drawing upon the results of two fixed target experiments: LSND and MiniBooNE. These experiments possess some of the largest datasets available, and both have published analyses of elastic scattering between neutrinos and electrons or nucleons. Due to their respective beam energies and methods of event detection, both LSND and MiniBooNE are sensitive to electron scattering, while only MiniBooNE is sensitive to nucleon scattering. Note also that LSND's beam energy was too low to produce mesons heavier than the pion in any significant quantities [5], and thus will not be able to probe the scenario using the η decay mode. MiniBooNE, with its much higher beam energies, produces η's in quantities large enough to warrant investigation.

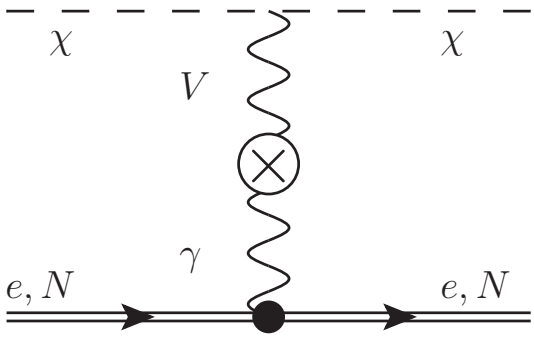

Figure 3.1: Scattering between scalar dark and ordinary matter in the U(1)′ hidden sector scenario.

3.2 Fixed Target Neutrino Experiments

We pause here to provide a brief description of the LSND and MiniBooNE experiments and some relevant quantities necessary for our analysis in section 3.3. The primary objective of these fixed target neutrino experiments was to confirm the existence of neutrino oscillations, which is in turn evidence for non-zero neutrino masses. A neutrino beam is generated by impacting a beam of protons onto a target (the composition of which varies with experiment), producing a beam secondary particles whose own decays produce copious numbers of neutrinos that propagate to the detector. Neutrino oscillations are studied by determining the number of neutrinos of each flavour that were generated at the neutrino source, and comparing it with the recorded number of each flavour that interact with the detector material. An excess or reduction in the number of neutrinos of any flavour reaching the target would then be indicative of neutrino oscillations [5]. This requires a thorough understanding of both the neutrino source and the backgrounds involved, the latter of which are often reduced through clever choice of the detector's position with respect to the target and beam axis. In the remainder of this section, we provide a few additional details specific to LSND and MiniBooNE.

3.2.1 A Few Comments About LSND

The Liquid Scintillator Neutrino Experiment, or LSND, was an experiment at Los Alamos National Laboratory that ran from 1993 to 1998. Over the lifetime of the experiment, the collaboration delivered 1.8×10^{23} protons on target (POT) with a kinetic energy of 798 MeV. The experiment used a water target from 1993 to 1995

(delivering 9.23×10^{22} POT), and a target made from an unspecified high-Z metal from 1996 to 1998 (delivering the remaining 8.22×10^{22} POT) [5]. With such a large dataset, LSND has the potential to impose very stringent limits on the parameter space of the scenario for the range of m_V to which it is sensitive.

The detector itself was an 8.3 m long cylinder with a diameter of 5.7 m. The detector was filled with mineral oil, which we will approximate as CH_2, with a small amount of added scintillant. Events were detected through a combination of Cherenkov radiation and scintillation light. The center of the detector was located 30 m downstream from the target, and 7.5 m below the beam axis (See Fig. 3.2) [63]. The majority of the neutrino flux at LSND was the result of the decays $\pi^+ \to \mu^+\nu_\mu$ and $\mu^+ \to e^+\nu_e\bar{\nu}_\mu$, most of which occurred at rest [5]. The off-axis positioning of the detector decreased the background, while not actually suppressing the neutrino flux as the majority of the neutrinos were produced isotropically.

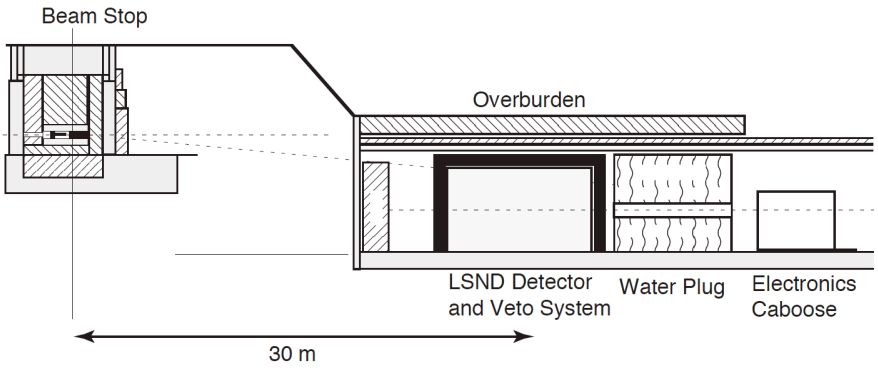

Figure 3.2: The LSND detector and target [5]. Copyright © 2001 by The American Physical Society.

3.2.2 A Few Comments About MiniBooNE

The Mini Booster Neutrino Experiment, or MiniBooNE, is an experiment at Fermilab that has been running since 2002, and has plans to continue taking data until March 2012. It was commissioned as a follow-up to LSND, with the goal of independently verifying (or refuting) the LSND anomaly, an excess in the recorded number of antineutrino events [5]. MiniBooNE has so far delivered $\mathcal{O}(10^{21})$ POT with a kinetic energy of 8 GeV [64]. As the experiment is still generating data, we have refrained from citing too precise a number. The experiment has used a beryllium target for the

entirety of its lifetime. While MiniBooNE has a much smaller dataset than LSND, its ability to probe a wider range of V and χ masses through the η decay mode makes the calculation of its sensitivity to the hidden sector scenario a worthwhile endeavor.

The MiniBooNE experiment employs a magnetic focusing horn to select for either positively or negatively charged mesons, focusing the selected charge along the beam axis while excluding the other charge, and in turn allowing the collaboration to select for neutrinos or antineutrinos. The horn is followed by a 50 m pion decay volume where most of the mesons decay in flight. The primary sources of the neutrinos at MiniBooNE are the charged pions, though the kaons also make a significant contribution [64].

The detector is a sphere with a radius of 6.1 m, though only an inner region with a radius of 5.75 m provides signal. The 0.35 m outer shell serves as a veto region, and tracks incident charged particles. The center of the detector is located 541 m downstream from the target, and 1.9 m below the beam axis [64] (see Fig. 3.3 for a diagram of the detector). Much like LSND, the detector is filled with mineral oil, which we will again approximate as CH_2. Scattering events are detected primarily through Cherenkov radiation, though nucleon scattering events are found through the absence of Cherenkov light, instead relying on scintillation light from fluors present in the mineral oil [65].

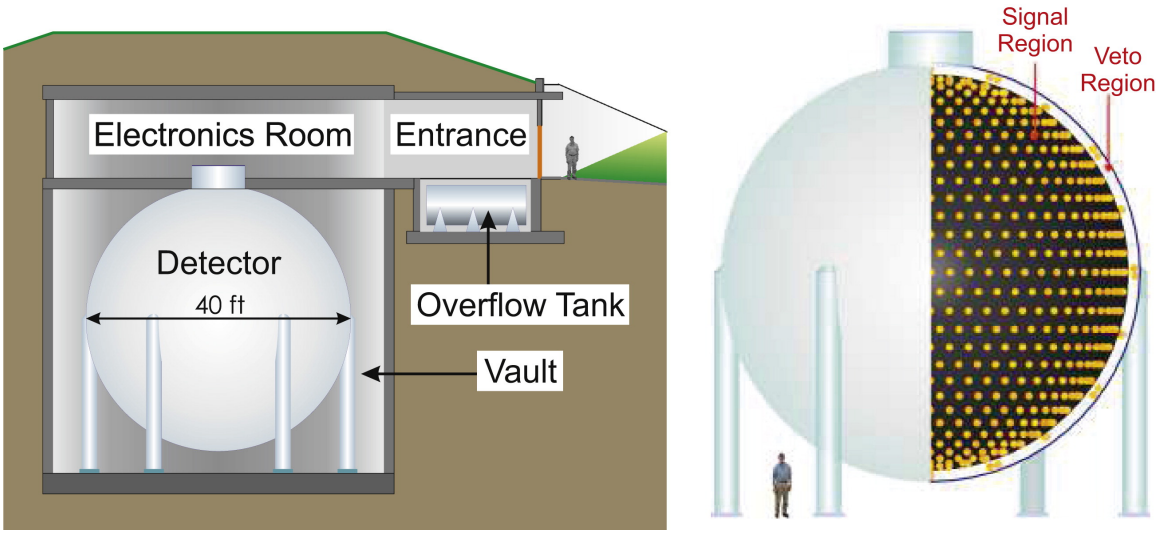

Figure 3.3: The MiniBooNE detector [6]. Copyright © 2009 Nuclear Instruments and Methods in Physics Research

3.3 Analysis

We begin by giving a brief outline of our analysis strategy. Our end goal is to calculate the number of dark matter scattering events expected by LSND and MiniBooNE, N_{events}, over the accessible parameter space of the hidden sector scenario set out in section 2.4 to within a factor of $\mathcal{O}(1)$, and then compare it to the number of neutral current scattering events actually recorded. To accomplish this goal, we need to answer three questions for each experiment:

- How many dark matter particles would have been produced under the U(1)′ hidden sector scenario?
- What is the probability that a dark matter particle so produced will reach the experiment's detector?
- How likely are the dark matter particles that reach the detector to produce a scattering event?

Each question will be addressed in turn for both LSND and MiniBooNE over the remainder of this chapter. We will answer the first question by relating the dark matter production rate to the π^0 and η production rates. For the second question, we will build a Monte Carlo simulation to determine the angular distributions of the produced dark matter, how much of it passes through the detector, and the energy distribution of the dark matter that reaches the detector. We will end by calculating the cross-sections for neutral current-like scattering events involving dark matter, developing a method of weighting the events generated by our simulation, and writing down an expression for the number of dark matter scattering events expected at an experiment for a given set of scenario parameters (m_χ, m_V, κ). Note that while the scenario actually contains four model parameters, we can write α' in terms of the other three using (2.21). This is discussed further in section 3.3.5.

3.3.1 Dark Matter Production at LSND

A brief glance at the chain of decay and production processes required for the production of a dark matter beam laid out in section 3.1 reveals that the dark matter flux scales linearly with the flux of the neutral mesons from which it is produced. For the case of LSND, we need to determine the number of π^0's produced over the

lifetime of the experiment, N_{π^0}. Unfortunately for our interests, the LSND collaboration did not need to record or simulate the π^0 production rate as π^0's are not a significant source of neutrinos and do not appreciably contribute to the experiment's background. Calculating N_{π^0} directly from proton interactions in the target to any great precision would be a daunting task. In practice, it is much simpler to estimate N_{π^0} by approximating the π^0 production rate with that of π^+, such that $N_{\pi^0} \simeq N_{\pi^+}$. We feel this approximation is reasonable as the measured π^+ and π^0 production rates in proton-nucleon collisions only differ by factors of $\mathcal{O}(1)$ (see eg. [66]).

We are now left with the task of estimating N_{π^+}, which we will accomplish by working backwards from the neutrino flux reported by the LSND collaboration. As noted before, the majority of the neutrinos produced at LSND were the products of π^+ decays at rest [5]. As these neutrinos are produced isotropically, and $\mathrm{Br}_{\pi^+\to\mu^+\nu_\mu} \simeq 1$, we find the following expression

$$N_{\pi^+} = \frac{\Phi_\nu \times A_{\mathrm{det}}}{(d\Omega_{\mathrm{lab}}/4\pi)_\nu} \sim 10^{22}, \tag{3.2}$$

where $\Phi_\nu = 1.3 \times 10^{14}\ \nu\ \mathrm{cm}^{-2}$ is the neutrino flux over the lifetime of the experiment, $A_{\mathrm{det}} \simeq 2.5 \times 10^5\ \mathrm{cm}^2$ is the area of the detector facing the target, and $(d\Omega_{\mathrm{lab}}/4\pi)_\nu \simeq 3 \times 10^{-3}$ is the fraction of the solid angle subtended by the detector relative to the target. Note that while (3.2) can be simplified to

$$N_{\pi^+} = \Phi_\nu \times 4\pi D_{\mathrm{det}}^2,$$

where D_{det} is the distance between the detector and the target, we find that (3.2) is clearer conceptually, and is straightforward to adapt for the boosted neutrino beam we will see in the following MiniBooNE discussion.

3.3.2 Dark Matter Production at MiniBooNE

To determine the dark matter production rate at MiniBooNE, we will need to estimate the production rates for both the π^0 and the η. For N_{π^0}, we will adopt a similar approach to that used for LSND, as π^0's were not simulated or recorded by MiniBooNE. We also note here that we will only be using the data from the neutrino mode run of the experiment, as MiniBooNE is still in the process of producing antineutrino data as of Summer 2011. The main difference between MiniBooNE and LSND for the purposes of this calculation is that the majority of pions decayed in

flight rather than at rest. We can adapt (3.2) to a boosted neutrino beam by Lorentz boosting into the pion center of mass frame before performing the calculation. In performing this boost, we replace the fractional solid angle in the lab frame with the fractional solid angle in the pion center of mass frame, $d\Omega_{\rm cm} \simeq \gamma^2 d\Omega_{\rm lab}$, though we should note that this relation only holds for small angles. The average energy of a π^+ produced at the MiniBooNE target was 1.12 GeV [64], and accordingly, we adopt $\gamma \simeq 8$ for the calculation of N_{π^+} at MiniBooNE,

$$N_{\pi^+} = \frac{\Phi_\nu \times A_{\rm det}}{\gamma^2 (d\Omega_{\rm lab}/4\pi)_\nu} \sim 1.7 \times 10^{20}, \tag{3.3}$$

where $A_{\rm det} \simeq 1.2 \times 10^6$ cm^2, $\Phi_\nu = 2.9 \times 10^{11}$ ν cm^{-2} and $(d\Omega_{\rm lab}/4\pi)_\nu \simeq 3.2 \times 10^{-5}$. This is actually a significant overestimate of the pion production rate due to the effect of MiniBooNE's magnetic focusing horn. Fortunately, the influence of the horn is easy to isolate as the MiniBooNE collaboration ran the experiment with the horn off for two weeks in April of 2004 [67]. It was noted that the neutrino flux dropped by a factor of six with the horn off, and we will reduce our pion production estimates accordingly. With the effect of the horn taken into account, we find the following estimate for the number of π^0's produced at MiniBooNE,

$$N_{\pi^0} \simeq 2.8 \times 10^{19}.$$

As noted earlier, the MiniBooNE proton beam, with a kinetic energy approximately ten times that of LSND, is capable of producing η's in significant numbers. As with the π^0's, η's are not an appreciable source of neutrino signal or background, and the MiniBooNE collaboration did not study their production. We will instead use experimental data to obtain an estimate for the η production cross-section, and use it to normalize the number of η's produced over the lifetime of the experiment to N_{π^0}. Drawing upon the results of Teis *et* al. [66], we estimate that for energies near that of the MiniBooNE proton beam

$$\frac{\sigma_{pp\to pp\pi}}{\sigma_{pp\to pp\eta}} \simeq 30, \tag{3.4}$$

and accordingly arrive at an estimate of the number of η's produced over the lifetime of the experiment,

$$N_\eta \simeq 9 \times 10^{17}.$$

3.3.3 Simulating a Dark Matter Beam at LSND

We wrote a simple Monte Carlo in order to determine the proportion of dark matter particles that reach the detector and the energy distribution of those particles. In the following section, we will discuss the process by which LSND is simulated in some detail. While the workings of the LSND and MiniBooNE simulations are very similar, there are also some important differences. These differences will be discussed in section 3.3.4.

Pions produced in LSND's target can possess a wide range of momenta, and can be emitted at almost any angle, though some angles and momenta are considerably more probable than others. As mentioned in section 3.1, the π^0's decay almost immediately, and we will assume that they always decay in flight. The V should also decay very rapidly, if perhaps not quite as quickly as the π^0 depending on the exact scenario paramaters, and we will assume that neither has time to propagate out of the target before decaying into dark matter particles. The simulation generates pions by iterating over probable angles and pion momenta. We work in spherical coordinates with the proton beam axis lying parallel to the z-axis, and iterate through θ, ϕ and the magnitude of the pion's three-momentum p_{π^0}.

For results presented later in Chapter 4, we iterate over $\theta_{\pi^0} \in [0, 1.8]$ radians with stepsize $\delta\theta_{\pi^0} = 0.05$ radians, then over $\phi_{\pi^0} \in [0, 2\pi)$ radians with stepsize $\delta\phi_{\pi^0} = 0.05$ radians and finally over pion momenta p_{π^0} over the range $p_{\pi^0} \in [0, 0.75]$ GeV with stepsize $\delta p_{\pi^0} = 0.02$ GeV. These limits have been chosen so as to keep the simulation run time short while maintaining a good resolution and finding most of the particle trajectories which cross through the detector. The upper limit of the θ iteration was chosen so as to cover more than 99% of the trajectories that pass through the detector while not having to cover the entire π^0 momentum space.

Each pion so generated is decayed into a γ (which is immediately discarded) and a V, the latter of which is then decayed into two χ's. The two χ's are generated in the V's rest frame, beginning with the four-vector for one of the χ's,

$$p^{\mu}_{\chi_1} = \left(\sqrt{m_\chi^2 + \mathbf{p}^2_{\chi_1}}, |\mathbf{p}_{\chi_1}| \cos\phi \sin\theta, |\mathbf{p}_{\chi_1}| \sin\phi \sin\theta, |\mathbf{p}_{\chi_1}| \cos\theta\right),$$

where $|\mathbf{p}_{\chi_1}| = \frac{1}{2}\sqrt{m_V^2 - 4m_\chi^2}$, and we have chosen the direction by generating random numbers $\phi \in [0, 2\pi)$ and $\cos\theta \in [-1, 1]$ in order to simulate the isotropic emission of χ's in the V rest frame. We generate the second χ's four-vector by applying a parity

transformation matrix, $P = \text{diag}(1, -1, -1, -1)$, to $p^{\mu}_{\chi_1}$.

The V's energy and propagation direction are determined by a method similar to that used for χ_1, with the V momentum defined as $|\mathbf{p}_V| = (m_\pi^2 - m_V^2)/(2m_\pi)$ and the angles chosen randomly over the same ranges. The next step is to boost the χ_1 and χ_2 four vectors from the V rest frame to the lab frame. This is done in two steps, first boosting from the V rest frame to the π^0 rest frame, then from there to the lab frame. The Lorentz boosts are performed by rotating the coordinate system such that the π^0 or V's direction of propagation lies parallel to the x-axis (depending on which boost is being performed), boosting by the appropriate β along the x-axis, and then performing the inverse rotation of the coordinate system. Once we have generated lab frame four-vectors for the two dark matter particles, we can use them to determine if the χ's that make up the dark matter beam propagate to the detector.

We use an admittedly crude technique to determine if a dark matter particle passes through the LSND detector. We define a function $f(x, y, z)$ which accepts a set of spatial coordinates and evaluates to 1 if these coordinates are inside the detector. More precisely,

$$f_{\text{LSND}}(x, y, z) = \begin{cases} 1 & : \sqrt{x^2 + (y + 4.65 \text{ m})^2} < 2.5 \text{ m and } z \in [25.85, 34.15] \text{ m} \\ & \text{and } y > -5.85 \text{ m} \\ 0 & : \text{Otherwise} \end{cases}$$

We sum $f(x, y, z)$ over 250 coordinate points along the particle trajectory, and normalize by the distance between the points (10 cm) tested. If this returns a number larger than zero, the particle passed through the detector, and it is recorded in a data file. Each χ that passes through the detector has its energy and the distance traveled within the detector recorded. In addition, we record p_{π^0} and θ_{π^0} for later weighting purposes (see section 3.3.5), and to enable later reconstruction of an event (primarily used for troubleshooting purposes) we record the χ propagation angles in the V rest frame, the V propagation angles in the π^0 rest frame, ϕ_{π^0}, and the masses m_V and m_χ.

3.3.4 Simulating a Dark Matter Beam at MiniBooNE

The process for simulating the dark matter beam at MiniBooNE is quite similar to that used for LSND. There is no practical difference between producing a dark matter beam from π^0 decays and η decays, and anything said about π^0's in this section will

also hold for η's.

Similarly to LSND, we assume that the π^0 and V decay before they have a chance to propagate beyond the target. All decays are also assumed to be in flight, an assumption that should hold true for the grand majority of dark matter particles produced. The simulation follows the same iteration procedure as LSND with the following limits: $p_{\pi^0} \in [0.02, 6]$ GeV with stepsize $\delta\phi_{p_{\pi^0}} = 0.02$ GeV, $\theta_{\pi^0} \in [0, .25]$ radians with stepsize $\delta\theta_{\pi^0} = 0.0025$ radians, and $\phi_{\pi^0} \in [0, 2\pi)$ radians with stepsize $\delta\phi_{\pi^0} = 0.4$ radians. The generation of χ's, and their subsequent boost to the lab frame was performed in a manner identical to that used for LSND.

One major difference between the two simulations lies in the method of determining whether a dark matter particle crosses through the detector or not. The MiniBooNE detector is spherical rather than cylindrical, and an analytical expression for the distance traveled through the detector is fairly simple to derive based on the distance of a line segment (the particle trajectory) to a point (the center of the detector). We will use the momentum three vector of the dark matter particle $\mathbf{p}_\chi$, and a vector pointing to the center of the detector, $\mathbf{p}_{\text{Det}} = (0, -1.9\text{m}, 541\text{m})$, to solve for the points at which the particle enters and exits the detector. This condition breaks down to a quadratic formula,

$$(\mathbf{p}_\chi)^2 x^2 - 2\,(\mathbf{p}_\chi \cdot \mathbf{p}_{\text{Det}})\, x + (\mathbf{p}_{\text{Det}})^2 = R_{\text{fid}}^2. \tag{3.5}$$

where R_{fid}=5 m is the radius of the fiducial volume of the MiniBooNE detector used by the MiniBooNE NCE scattering analysis [65]. The points of intersection are given by $x_\pm \mathbf{p}_\chi$, where $x_\pm$ are the solutions to 3.5. So long as $x_\pm$ are real and positive, the χ passes through the detector, and the distance traveled through the detector by the particle is $L = |(x_+ - x_-)\mathbf{p}_\chi|$.

3.3.5 Calculating N_{Events} at LSND

Now that we have run the LSND dark matter beam Monte Carlo for a set of m_χ and m_V, we can use the results of the simulation to estimate the number of dark matter scattering events that would be expected for a given κ. The goal is to generate a quantity representing the average cross-section of all the dark matter particles which reach the detector. We will calculate this quantity from all of the dark matter particle trajectories that reached the detector in the simulation. We will need to weight each trajectory by the momentum and angular distribution of the π^0 from

which it originated. As has been mentioned several times before, LSND had no need to study the production of π^0, and so no parametrization of the π^0 distribution for LSND exists. We instead make the assumption that it will be proportional to the production distribution of π^+'s to within a factor of $\mathcal{O}(1)$, and use the parametrization of the π^+ production cross-section by Burman and Smith [68].

The parametrization is based on two studies of the pion-production cross-section with proton beam kinetic energies of 585 MeV and 730 MeV. The parametrization can be safely extrapolated to the beam energies used at LSND, and can be adapted to a number of different target materials. This is particularly useful for LSND, as two different target materials were used over the course of the experiment. We label the parameterization of Burman and Smith as $d\sigma_{\mathrm{B,S}}(\theta, p_{\pi^0}, Z, T_P)$, where Z is the atomic number of the target material and T_P is the kinetic energy of the proton beam impacting on the target. We will actually be using two rescaled versions of the parametrization (one for each target material), which will accept an angle and a pion kinetic energy as inputs. We define the distribution for pions produced during the 1993-1995 water target run as

$$f_{\mathrm{H_20}}(\theta, p_{\pi^0}) = \frac{2d\sigma_{\mathrm{B,S}}(\theta, p_{\pi^0}, Z = 1, 800\mathrm{MeV}) + d\sigma_{\mathrm{B,S}}(\theta, p_{\pi^0}, Z = 8, 800\mathrm{MeV})}{N_8 + 2N_1}, \quad (3.6)$$

and for the pions produced during the 1996-1998 High-Z metal run,

$$f_{\text{High-Z}}(\theta, p_{\pi^0}) = \frac{d\sigma_{\mathrm{B,S}}(\theta, p_{\pi^0}, Z = 70, 800\mathrm{MeV})}{N_{70}}, \quad (3.7)$$

where we define N_i as follows,

$$N_i = \int_0^{\pi} d\theta \int_{0\text{ GeV}}^{0.75\text{ GeV}} dp_{\pi^0} d\sigma_{\mathrm{B,S}}(\theta, p_{\pi^0}, Z = i, 800\text{ MeV}). \quad (3.8)$$

As we already have an estimate for the number of π^0's produced at LSND from section 3.3.1, we will be using the pion distribution to weight the relative likelihood of a pion being produced with some angle and momentum. In order to simplify the process of calculating the contribution of each dark matter trajectory to the predicted number of events, we normalize the distribution to unity by dividing them by normalization factors N_i,

$$\int_0^{\pi} d\theta \int_{0\text{ GeV}}^{0.75\text{ GeV}} dp_{\pi^0} f_{\mathrm{H_20}}(\theta, p_{\pi^0}) = \int_0^{\pi} d\theta \int_{0\text{ GeV}}^{0.75\text{ GeV}} dp_{\pi^0} f_{\text{High-Z}}(\theta, p_{\pi^0}) = 1.$$

The distribution is not dependent upon ϕ, and the normalization over any ϕ integral or sum will be handled seperately. You may notice that we have chosen $Z = 70$ for the High-Z metal run, even though it is unlikely that Ytterbium was used to construct the target. However, as we do not know the actual metal (or metals) used in the target and the Burman and Smith parametrization remains fairly constant with increasing Z for sufficiently large Z (see Fig. 3.4 for examples), the precise large integer chosen for the atomic number is of little importance.

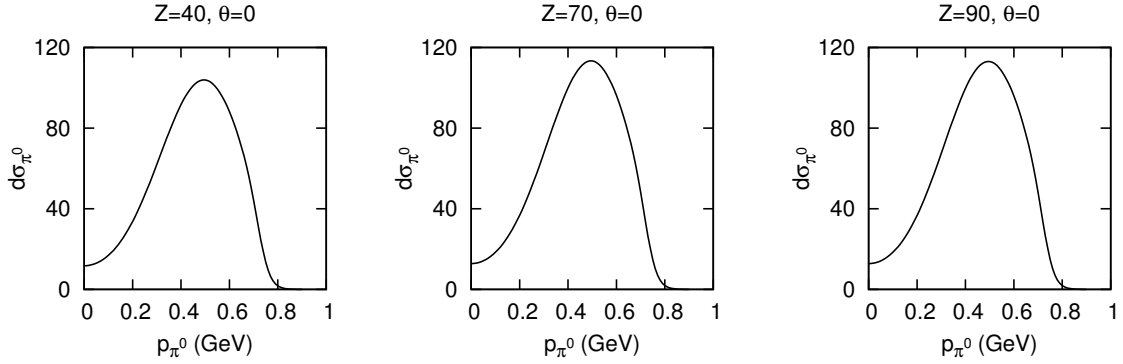

Figure 3.4: Examples of the Burman and Smith pion parametrization used in the weighting of our LSND simulation results for large values of Z. The distribution changes little in shape or magnitude for large Z.

We also need to determine the likelihood that a neutral current-like elastic scattering event will occur when a dark matter particle passes through the detector. The scattering cross-section for $e\chi \to e\chi$, assuming that $E \gg m_e$, takes the form

$$\frac{d\sigma_{e\chi\to e\chi}}{dE_f} = \frac{\alpha'\kappa^2}{\alpha} \times \frac{4\pi\alpha^2\left(2m_e(E^2 - EE_f) - m_\chi^2 E_f\right)}{E^2(m_V^2 + 2m_e E_f)^2}, \tag{3.9}$$

where E is the energy of the incoming dark matter particle and E_f is the energy of the scattered electron. We use (2.21) to replace the ratio $\frac{\alpha'\kappa^2}{\alpha}$ with an expression in terms of m_V and m_χ,

$$\frac{\alpha'\kappa^2}{\alpha} \sim 3 \times 10^{-4}\text{GeV}^{-2} \times \frac{(-m_V^2 + 4m_\chi^2)^2}{m_\chi^2\sqrt{1 - \frac{m_e^2}{m_\chi^2}}}, \tag{3.10}$$

where we have converted from MeV to GeV. Now that we have derived a differential cross-section in terms of E, E_f, m_V and m_χ, we need to integrate it over the allowed values of E_f. The limits on E_f will be determined by kinematics and the momentum

cuts imposed by LSND. For elastic electron neutrino scattering, the collaboration only accepted events for which $E_f \in [18, 50]$ MeV in order to reduce the background in elastic scattering [69]. We match these cuts in order to produce results that can be easily compared with the number of elastic scattering events reported by LSND. In addition, conservation of energy and momentum limits the maximum recoil electron energy to

$$E_{f,\max} = \frac{m_e(E + m_e)}{m_e + E - \sqrt{E^2 - m_\chi^2}}. \tag{3.11}$$

Dark matter trajectories for which $E_{f,\max} < 20$ MeV are immediately discarded, as they would not survive the LSND momentum cuts.

To each dark matter particle generated in the simulation that passed through the detector we now assign the following quantity,

$$V_{\text{LSND},i} = \sigma_{e\chi\to e\chi}(E_i) \times L_i \times \frac{W_1 f_{\text{H}_2\text{0}}(\theta_i, p_i) + W_2 f_{\text{High-Z}}(\theta_i, p_i)}{W_1 + W_2}, \tag{3.12}$$

where $W_1 = 7.38 \times 10^{13}$ ν cm^{-2} and $W_2 = 5.18 \times 10^{13}$ ν cm^{-2} are the neutrino fluxes delivered during the water target and High-Z metal runs [5], respectively, L_i is the distance the trajectory passed through the detector and E_i is the energy of the dark matter particle. θ_i and p_i correspond to θ_{π^0} and p_{π^0} (defined at the end of section 3.3.3) of the π^0 whose decay produced this dark matter particle. The quantity V_{LSND} is a sort of effective volume for the dark matter particle's interactions with the detector, containing both the cross-section and the distance passed through the detector. This is then weighted by the likelyhood that the orinigal π^0 that decayed into this dark matter particle would be produced at all. As this pion could have been produced during either the water target or High-Z metal target runs, we need to include both pion distributions. Since the integrated neutrino flux, and therefore the pion production, was larger for the water target than the High-Z metal target, we take a weighted average of the two distributions and weight the water target run more heavily.

We are now prepared calculate N_{events} for a set of scenario parameters (m_χ,m_V,κ). We write it using the sum of the effective volumes of all the particles which passed through the detector in the simulation,

$$N_{\text{events}} = n_e \times N_{\pi^0} \times \text{Br}_{\pi^0\to V\gamma} \times \epsilon_{\text{eff}} \times \sum_i V_{\text{LSND},i} A_{\pi^0}. \tag{3.13}$$

Here $n_e = 5.1 \times 10^{23}$ electrons cm^{-3} is the number density of electrons in the LSND detector, N_{π^0} was estimated in section 3.3.1 to be 10^{22}, $\mathrm{Br}_{\pi^0 \to V\gamma}$ was defined in (3.1), V_{LSND} was derived earlier in (3.12), $\epsilon_{eff} \simeq 0.19$ is the efficiency with which LSND detects elastic electron scattering events [5], and $A_{\pi^0} = \delta\theta\delta\phi\delta p_{\pi^0}/(2\pi)$, where $\delta\theta$, $\delta\phi$ and δp_{π^0} are the step sizes used during the dark matter beam simulation described in section 3.3.1.

We will take a moment to justify the form of (3.13). It is quite apparent that N_{π^0} tells us the number of the pions we have to work with, and combining it with $\mathrm{Br}_{\pi^0 \to V\gamma}$ tells us the number of V's, and ultimately χ's, that have been produced over the lifetime of the experiment. The sum over the effective volume $V_{\mathrm{LSND},i}$ requires more explanation. We use $\sum_i V_{\mathrm{LSND},i} A_{\pi^0}$ to describe the probability that a dark matter particle produced from a single, random pion will pass through the detector and interact with an electron in such a way as to be recorded by the experimental apparatus as an elastic scattering event. We use a sum because we generate these dark matter trajectories at distrete points in the pion's momentum space. Each point in momentum space actually represents a small volume, and, as integrating (3.8) is quite difficult and time-consuming, we make the following approximation,

$$\int_{\theta-\delta\theta/2}^{\theta+\delta\theta/2} d\theta' \int_{p_{\pi^0}-\delta p_{\pi^0}/2}^{p_{\pi^0}+\delta p_{\pi^0}/2} dp'_{\pi^0} f(\theta', p'_{\pi^0}) \simeq f(\theta, p_{\pi^0})\delta p_{\pi^0}\delta\theta, \tag{3.14}$$

for small $\delta\theta$ and δp_{π^0}. While the combination of pion parametrization and the relevant step size will normalize a sum over θ_{π^0} and the pion momentum to unity, they do not take the ϕ_{π^0} sum into account. We divide the sum by a final factor of 2π to finish the normalization.

We are not quite done yet, though. In order to make useful and readable plots of the scenario parameter space, we pick a value of m_χ to test, and then run the simulation over an array that covers all possible values of m_V. For the plots presented in Chapter 4, we used a step size of $\delta m_V = 5$ MeV, and tested $m_\chi = 1$, 10, 50 and 100 MeV. The datasets for each value of m_V tested were weighted using (3.12). The expected number of events for an arbitrary value of m_V was then calculated by taking a weighted average of $\sum_i V_{\mathrm{LSND},i}$ for the two nearest V masses for which the simulation was run.

3.3.6 Calculating N_{Events} at MiniBooNE

The calculation of N_{events} for MiniBooNE will closely mirror that of LSND, though with significant differences at several of the steps along the way. The first step is to find a π^0 production distribution for MiniBooNE, which, unsurprisingly, does not actually exist. The collaboration does, however, provide a parametrization for π^+ and π^- production using the Sanford and Wang fit [64], which we will label quite appropriately as $d\sigma_{\text{SW},\pi^+}$ for π^+ and $d\sigma_{\text{SW},\pi^-}$ for π^-. We will estimate the π^0 production distribution by averaging the π^+ and π^- parametrizations,

$$f_{\pi^0} = \frac{d\sigma_{\text{SW},\pi^+} + d\sigma_{\text{SW},\pi^-}}{N_{\text{Tot}}}, \tag{3.15}$$

where $d\sigma_{\text{SW},\pi^+}$ and $d\sigma_{\text{SW},\pi^-}$ are the Sanford-Wang fits for π^+ and π^- production, respectively, and N_{Tot} is a normalization factor similar to N_i defined in (3.8),

$$N_{\text{Tot}} = \int_0^{\frac{\pi}{2}} d\theta \int_{0\text{ GeV}}^{6\text{ GeV}} dp_{\pi^0} \left(d\sigma_{\text{SW},\pi^+} + d\sigma_{\text{SW},\pi^-}\right). \tag{3.16}$$

We normalize the Sanford and Wang pion parametrization for the same reason we normalized the Burman and Smith parametrization for LSND: We are not using this production distribution to predict the number of pions produced, but to determine the relative weighting we should assign to each pion. The distribution is, of course, normalized to unity,

$$\int_0^{\pi/2} d\theta \int_{0\text{ GeV}}^{6\text{ GeV}} dp_{\pi^0} f_{\pi^0}(\theta, p_{\pi^0}) = 1.$$

As with π^0's, there is no η production distribution, and so we will use (3.15) to weight η production as well as π^0 production.

We still need to determine the likelihood that a dark matter particle that reaches the detector will interact with the mineral oil in a manner detectable by the MiniBooNE collaboration. For electron scattering we will use (3.9) and (3.10) that we derived earlier. As MiniBooNE has not released an analysis of elastic neutral current electron scattering, we will not impose any momentum cuts apart from those forced upon us by the kinematics of the interaction, that is, the outgoing electron can take any energy between its rest mass and its maximum from (3.11).

As MiniBooNE uses a much higher beam energy than LSND and employs different event detection techniques, it is feasible to detect neutral current elastic scattering between neutrinos and nucleons. The collaboration has published a full analysis on

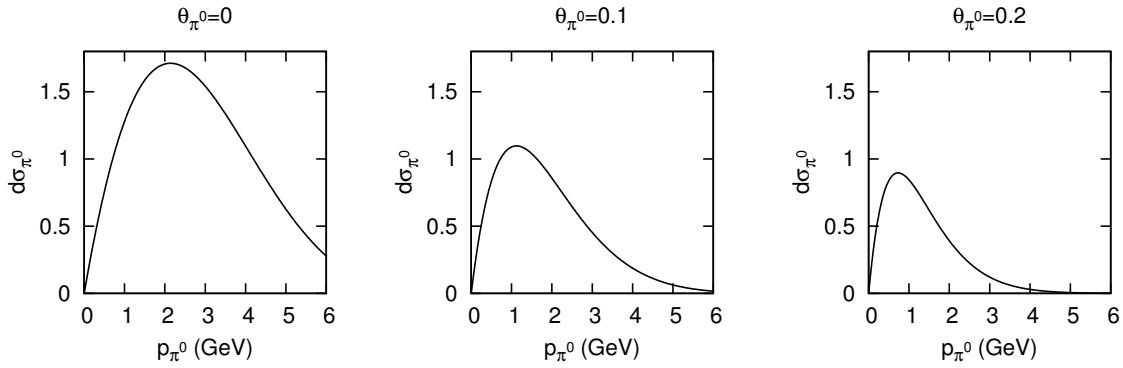

Figure 3.5: Examples of the rescaled Sanford and Wang pion parametrization used in our MiniBooNE analysis for various θ_{π^0}.

the subject using the data from their neutrino mode run [65]. In order to investigate this channel, we now calculate the differential cross-section for neutral current-like elastic scattering between dark matter and nucleons. This process is similar to the vector part of Z-mediated neutrino-nucleon elastic scattering (see eg. [70]), and we obtain the following differential cross-section,

$$\frac{d\sigma_{N\chi\to N\chi}}{dE_\chi} = \frac{\alpha'\kappa^2}{\alpha} \times \frac{4\pi\alpha^2\left[F_{1,N}^2(Q^2)A(E,E_\chi) - \frac{1}{4}F_{2,N}^2(Q^2)B(E,E_\chi)\right]}{\left(m_V^2 + 2m_N(E-E_\chi)\right)^2\left(E^2 - m_\chi^2\right)}, \tag{3.17}$$

where E and E_χ are the energies of the incident and outgoing dark matter particles, respectively, and $Q^2 = 2m_N(E - E_\chi)$ is the momentum transfer. The functions A and B are defined as

$$A(E,E_\chi) = 2m_N E E_\chi - m_\chi^2(E - E_\chi) \tag{3.18}$$

$$B(E,E_\chi) = (E_\chi - E)\left[(E_\chi + E)^2 + 2m_N(E_\chi - E) - 4m_\chi^2\right]. \tag{3.19}$$

The cross-section holds for both neutrons and protons so long as the appropriate nuclear form factors are used. We make use of the following monopole and dipole form factors

$$F_{1,N} = \frac{q_N}{(1 + Q^2/m_N^2)^2}, \quad F_{2,N} = \frac{\kappa_N}{(1 + Q^2/m_N^2)^2}, \tag{3.20}$$

where $q_p = 1$, $q_n = 0$, while $\kappa_p = 1.79$ and $\kappa_n = -1.9$. Equation (3.17) only describes the scattering cross-section for free nucleons, but in reality, dark matter will either be scattering off nucleons bound in a Carbon nucleus, or one of the two Hydrogen

nuclei of a CH_2 molecule. Following the MiniBooNE analysis [65], we can write an effective differential cross-section as follows,

$$\frac{d\sigma_{N\chi\to N\chi}}{dE_\chi} = \left[\frac{1}{7}C_{pf}(Q^2) + \frac{3}{7}C_{pb}(Q^2)\right]\frac{d\sigma_{\chi p\to\chi p}}{dE_\chi} + \frac{3}{7}C_{nb}(Q^2)\frac{d\sigma_{\chi n\to\chi n}}{dE_\chi}, \tag{3.21}$$

where the $C's$ describe MiniBooNE's efficiency for detecting scattering off one of the protons or neutrons bound in a carbon molecule or one of the protons making up the hydrogen nuclei. The efficiencies are dependent on the momentum transfer of the scattering, but are quite close to unity for $Q^2 \in [0.4, 1]$ GeV^2 [65]. We have not made a distinction between bound and free proton scattering cross-sections in (3.21) or our numerical analysis. In order to determine the full cross-section, we will integrate (3.21) over the range $Q^2 \in [0.1, 1.6]$ GeV^2, corresponding to the cuts used in the collaboration's neutral current neutrino nucleon scattering analysis. The lower limit means that our analysis will not be sensitive to elastic coherent nuclear scattering, and our nucleon-level cross-sections should be sufficient.

We can now combine our differential cross-sections with our simulation results to find an effective volume for each dark matter trajectory which passes through the detector. The electron treatment for MiniBooNE is quite similar to equation (3.12) that we used for LSND, though actually a bit simpler,

$$V_{e\phi,i} = \sigma_{e\chi\to e\chi}(E_i) \times L_i \times f_{\pi^0}(\theta_i, p_i), \tag{3.22}$$

where L_i is the distance traveled through the detector, and $\phi = \pi^0, \eta$ is the neutral meson which produced this particular dark matter event. The nucleon treatment is nearly identical, as we need only make the substitution $\sigma_{e\chi\to e\chi} \to \sigma_{N\chi\to N\chi}$,

$$V_{N\phi,i} = \sigma_{N\chi\to N\chi}(E_i) \times L_i \times f_{\pi^0}(\theta_i, p_i). \tag{3.23}$$

Note that we use the f_{π^0} distribution for both the η and π^0 cases, as mentioned earlier.

We can now combine all of the results of this section to estimate the number of neutral current-like elastic scattering events MiniBooNE would observe under our hidden sector scenario. The simulation must be run for dark matter produced from both η and π^0 decays for given m_V, as the mass of the decaying neutral meson has a significant effect on the kinematics of the beam. Of course, we need not run the π^0 simulation if $m_V > m_{\pi^0}$. For electron scattering, the expression is quite similar to

equation (3.13) used for LSND,

$$N_{e\text{ events}} = n_e \times \left(N_\pi^0 \mathrm{Br}_{\pi^0 \to V\gamma} \times \sum_i V_{e\pi^0,i} A_{\pi^0} + N_\eta \mathrm{Br}_{\eta \to V\gamma} \times \sum_j V_{e\eta,j} A_\eta \right), \quad (3.24)$$

where $n_e = 5.1 \times 10^{23}$ electrons cm^{-3} is the number density of electrons in the MiniBooNE detector, N_π^0 and N_η were estimated in section 3.3.2 to be 2×10^{19} and 9×10^{17}, respectively, $\mathrm{Br}_{\pi^0,\eta \to V\gamma}$ are defined in (3.1), and $A_\phi = \delta\theta\delta\phi\delta p_\phi/(2\pi)$, $\phi = \pi^0, \eta$, where $\delta\theta$, $\delta\phi$ and δp_ϕ are the step sizes used during the dark matter beam simulation (see section 3.3.4 for details). Remember that while the cross-section differs for protons and neutrons, this is accounted for in (3.21). The sum over i (j) counts all of the trajectories generated by the simulation of dark matter produced from π^0 (η) decays. As with the LSND calculation, we normalize the sum by 2π because the distribution f_{π^0} is not normalized for sums or integrals over ϕ.

The expression changes little for the number of nucleon scattering events,

$$N_{N\text{ events}} = 14 n_{\mathrm{CH_2}} \times \epsilon_{\text{eff}} \left(N_\pi^0 \mathrm{Br}_{\pi^0 \to V\gamma} \times \sum_i V_{N\pi^0,i} A_{\pi^0} + N_\eta \mathrm{Br}_{\eta \to V\gamma} \times \sum_j V_{N\eta,j} A_\eta \right), \quad (3.25)$$

where $n_{\mathrm{CH_2}} = 6.375 \times 10^{22}$ nucleons cm^{-3} is the number density of CH_2 in the MiniBooNE detector, ϵ_{eff}=0.59 is the efficiency of the MiniBooNE NCE nucleon scattering analysis, and the factor of 14 is introduced to account for the number of nucleons in a CH_2 molecule.

In this chapter, we described the process for generating a hidden sector dark matter beam at a fixed target collider, and provided the necessary details for calculating the effects of such a beam on the LSND and MiniBooNE fixed target neutrino experiments. We covered all of the steps involved in simulating the kinematics of a dark matter beam produced under this scenario, and the process followed for the calculation the expected number of dark matter scattering events using those simulations. In the next chapter, we will present and comment on the end results of this analysis.

Chapter 4

Results

In the last chapter, we discussed the methods by which we simulated the production of a dark matter beam at a fixed target neutrino experiment and calculated the number of neutral current-like scattering events that would be expected at one of these experiments for a given set of hidden sector scenario parameters (m_χ, m_V, κ). We have run our simulation over a series of possible m_V values for a given production channel (decays from π^0 or η) and m_χ, and then determined the number of events expected at a given experiment over the $m_V - \kappa$ parameter space. The results are presented in a series of plots below. Three regions are shown on each plot: A lightly shaded region for parts of the parameter space where we expect more than 10 events, a medium shaded region for where we expect more than 1000 events, and finally a darkly shaded region for where we expect more than 10^6 neutral current-like scattering events involving dark matter. We have plotted increasing values of κ along a logarithmic y-axis, and increasing values of m_V along the x-axis.

We have also plotted a black line to delineate the strong coupling boundary, where $\alpha' > 4\pi$. Specifically, we plot the function

$$\kappa = \sqrt{3 \times 10^{-10}\ \mathrm{MeV}^{-2} \times \frac{\alpha\left(4m_\chi^2 - m_V^2\right)^2}{m_\chi^2}}. \tag{4.1}$$

This equation plots a line in the $m_V - \kappa$ parameter space of the scenario where $\alpha' = 4\pi$. While this marks the regime where our perturbative calculations cease to be reliable, astronomical constraints on self-interactions would likely provide even stronger constraints. Regardless of the potential for astronomical observations to impose tighter constraints, we will take a conservative approach and only exclude

parameter space below the line marking the strong coupling boundary.

4.1 LSND

4.1.1 Dark Matter Electron Scattering From the π^0 Decay Channel

The first experiment examined was LSND, where it was hoped that with its large dataset we could impose stringent limits on the parameter space of the hidden sector scenario. In Fig. 4.1a, we have plotted the estimated number of neutral current-like scattering events for $m_\chi = 1$ MeV over the range $m_V \in [4, 134]$ MeV. This case was covered in an earlier analysis [16], and we find that our calculated sensitivity is consistent with their results. In order to actually exclude regions of the parameter space, we must compare our analysis with the number of elastic scattering events that were actually observed. As LSND observed $\mathcal{O}(200)$ elastic scattering events [69], we find that we can easily exclude the medium and darkly shaded regions for which we would expect LSND to produce more than a thousand events. These limits could be further improved by a spectral analysis of the energy of the recoiling electrons. The energy of the dark matter beam is considerably higher than that expected of a neutrino beam produced from pion and muon decays at rest, and correspondingly, recoil electrons from dark matter scatterings would be more energetic than those from the neutrino beam. We would then be able to compare our expected number of events with the far rarer neutrinos produced by pion decays in flight, of which LSND only observed $\mathcal{O}(10)$. Even without the spectral analysis, we find that we are able to exclude the majority of the parameter space for $m_V < m_{\pi^0}$ by combining the neutral current-like scattering results with the strong coupling condition.

In order to extend our analysis further and determine if LSND's high sensitivity still holds for larger hidden sector dark matter masses, we have performed the same calculation of expected neutral current-like scattering events for $m_\chi = 10$ MeV. In this case we plot over the range $m_V \in [24, 134]$ MeV, and the sensitivity drops by an order of magnitude, mostly due to suppression of the scattering cross section in (3.9) by a factor of m_χ^{-2} that appears in the expression for the ratio of $\alpha'\kappa^2/\alpha$ in (3.10). We increasingly restrict the m_V range because of our assumption that $m_V > 2m_\chi$ in this scenario. In addition, note that the strong coupling condition grows weaker with increased m_χ, as should be expected from the form of (4.1). Despite the weakening of

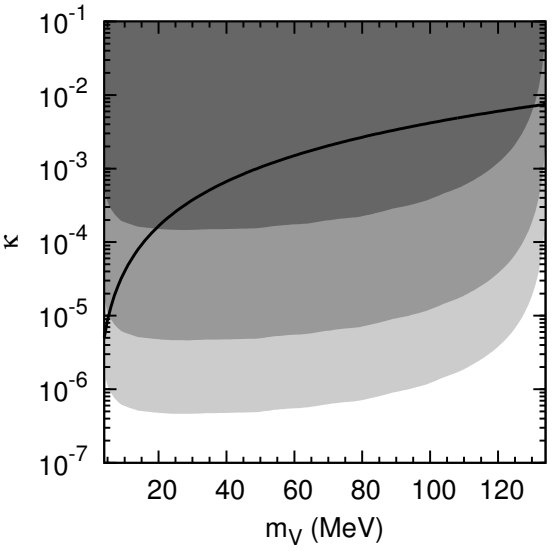

(a) $m_\chi = 1$ MeV

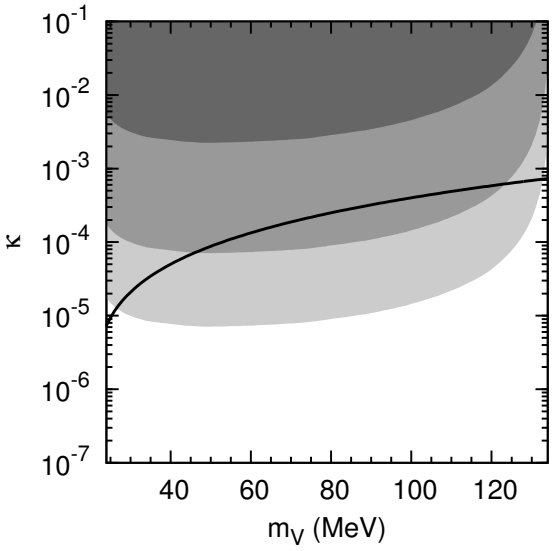

(b) $m_\chi = 10$ MeV

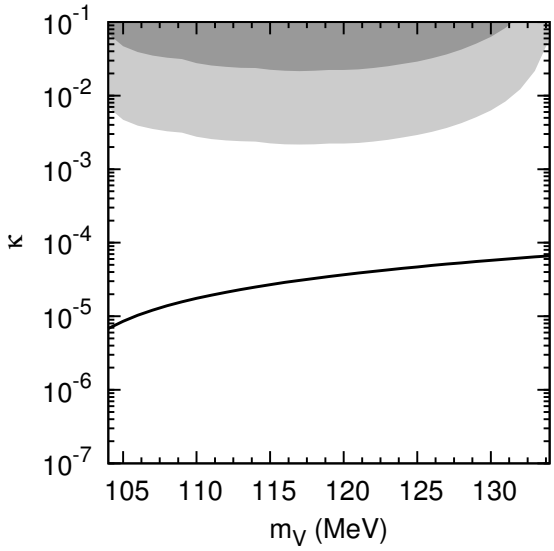

(c) $m_\chi = 50$ MeV

Figure 4.1: Expected number of neutral current-like dark matter electron scattering events at the LSND detector for three values of m_χ. The regions show greater than 10 (light), 1000 (medium) and 10^6 (dark) expected events. Areas below the black line correspond to $\alpha' > 4\pi$.

both the sensitivity of LSND and of the strong coupling condition, we can use LSND to exclude most of the parameter space for $m_\chi = 10$ MeV and $m_V < m_\pi^0$. We have also tested $m_\chi = 50$ MeV at LSND over $m_V \in [104, 134]$ MeV, and find that the sensitivity drops drastically. It appears that LSND's sensitivity drops substantially with increasing dark matter mass, as we can only place very weak constraints on the parameter space compared to the previous two cases. We should also note that the sensitivity decreased more than would be expected from a simple suppression by m_χ^{-2}, and kinematics from the simulation may be playing a role.

4.2 MiniBooNE

4.2.1 Dark Matter Electron Scattering From the π^0 Decay Channel

As there are a number of processes ($e\chi \to e\chi$ and $N\chi \to N\chi$) and decay channels ($\eta \to V\gamma$ and $\pi^0 \to V\gamma$) that could be used to detect a low mass hidden sector dark matter candidate at the MiniBooNE experiment, we have prepared four sets of plots to test the experiment's ability to probe the hidden sector parameter space. We begin with Fig. 4.2, where we have plotted the expected number of neutral current-like elastic scattering events between electron and dark matter produced by the π^0 decay channel for $m_\chi = 1$ MeV, 10 MeV, and 50 MeV over the same V mass ranges found in Fig. 4.1. These plots were made primarily to allow us to compare the sensitivity of MiniBooNE to LSND. We cannot use them to actually constrain the scenario parameter space, as MiniBooNE has not yet performed a neutral current elastic scattering analysis for electron neutrino scattering. These plots represent very optimistic estimates of MiniBooNE's possible sensitivity, as no momentum cuts have been imposed on the recoil energy of the outgoing electron. Comparing the $m_\chi = 1$ MeV and 10 MeV cases between LSND and MiniBooNE, we see that the sensitivity curves have similar shapes, but MiniBooNE's are weaker by about an order of magnitude. The $m_\chi = 50$ MeV case in Fig. 4.2c is a little more interesting in that it indicates that MiniBooNE has a slightly greater sensitivity than LSND, despite the latter's much higher number of POT. Despite this small gain in sensitivity, it is still very weak, and MiniBooNE is unlikely to be able to impose any constraints on the scenario parameter space that are significantly tighter than those of LSND for this decay channel and detection strategy.

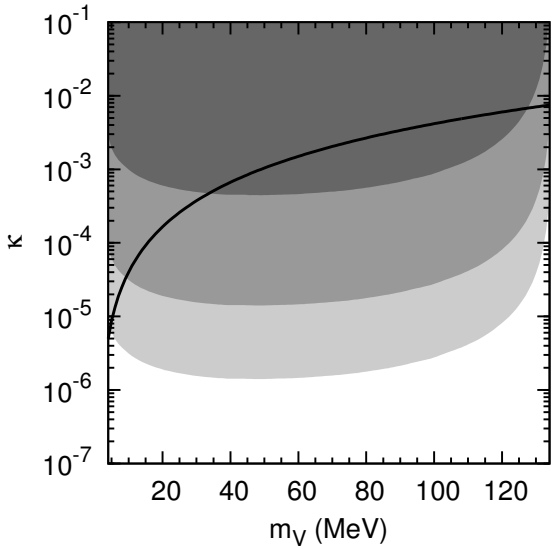

(a) $m_\chi = 1$ MeV

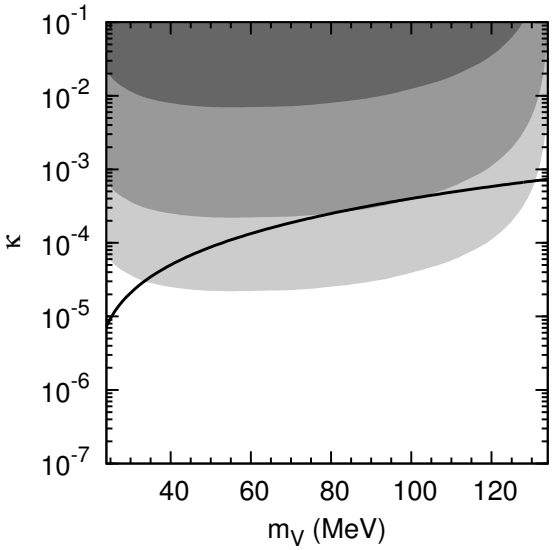

(b) $m_\chi = 10$ MeV

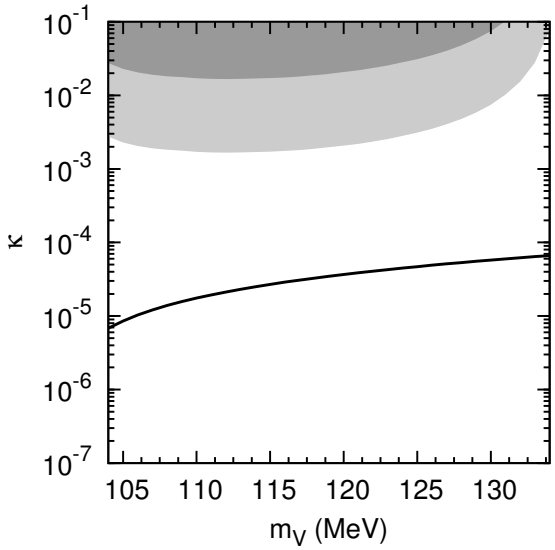

(c) $m_\chi = 50$ MeV

Figure 4.2: Expected number of neutral current-like dark matter electron scattering events at the MiniBooNE detector for three values of m_χ. These plots include only the contributions from π^0 decays. The regions show greater than 10 (light), 1000 (medium) and 10^6 (dark) expected events. Areas below the black line correspond to $\alpha' > 4\pi$.

4.2.2 Dark Matter Nucleon Scattering From the π^0 Decay Channel

In addition to electron scattering, we have also considered nucleon scattering. The next set of the plots in Fig. 4.3 were made primarily for comparison with the plots of Fig. 4.2 in order to get a handle on how MiniBooNE's sensitivity to elastic neutral current-like scattering between dark matter and nucleons differed from the same process with electrons. We will combine the π^0 and η results in the next set of plots of this section. It had been hoped that the cross section would scale with the mass of the scattered particle, and that we would see gains in the cross section on the order of the ratio between $m_N/m_e \sim 2000$, but a closer examination of equation (3.17) reveals that this gain would only be seen when $m_V^2 \gg Q^2$. We are instead working in the mass regime where $m_V^2 \ll Q^2$, though we should expect some small enhancement as m_V increases. We see in Figs. 4.3a and 4.3b that the sensitivity from nucleon scattering is of the same order of magnitude as that from electron scattering, though fairly heavily suppressed for low m_V. The $m_\chi = 50$ MeV case in Fig. 4.3c shows a slight gain in sensitivity from nucleon scattering over electron scattering. We should also note that the constraints from the MiniBooNE nucleon scattering case are not as strong as they may at first appear, as MiniBooNE observed between $\mathcal{O}(10^4)$ and $\mathcal{O}(10^5)$ events, depending on the momentum cuts employed [65]. We will be using the most generous momentum cuts, and therefore will begin excluding parameter space when the predicted number of events is greater than 10^5 events. We have included this condition as a dashed line on the plots for elastic neutral current-like scattering between nucleons and dark matter. As a result, the MiniBooNE analysis using dark matter from the π^0 decay channel cannot exclude any scenario parameter space that has not already been conclusively ruled out by the LSND analysis in the previous section. We will have to combine the results from dark matter produced in the η and π^0 decay channels to see the utility of the MiniBooNE sensitivity analysis.

4.2.3 Dark Matter Electron Scattering From the π^0 and η Decay Channels

We now combine the expected neutral current-like elastic scattering events between dark matter and electrons from the π^0 and η decay channels in Fig. 4.4. At low m_V, we can clearly see the pion contribution to the expected number of events as

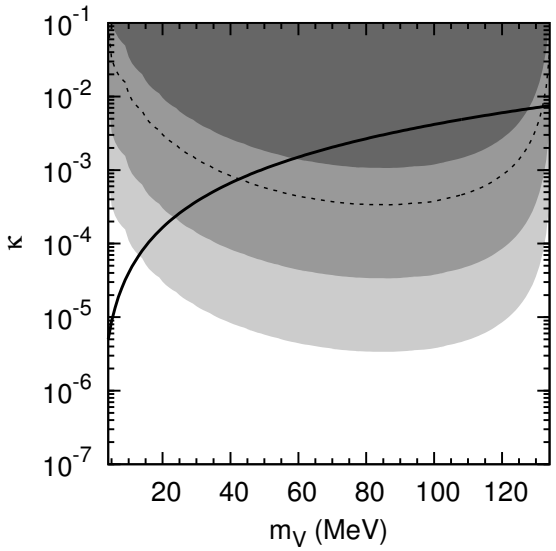

(a) $m_\chi = 1$ MeV

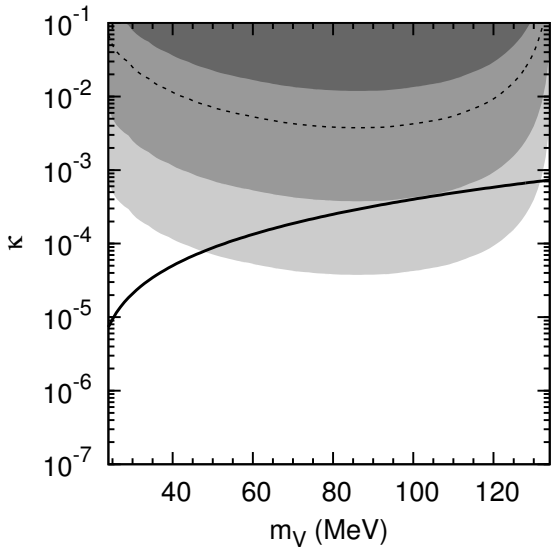

(b) $m_\chi = 10$ MeV

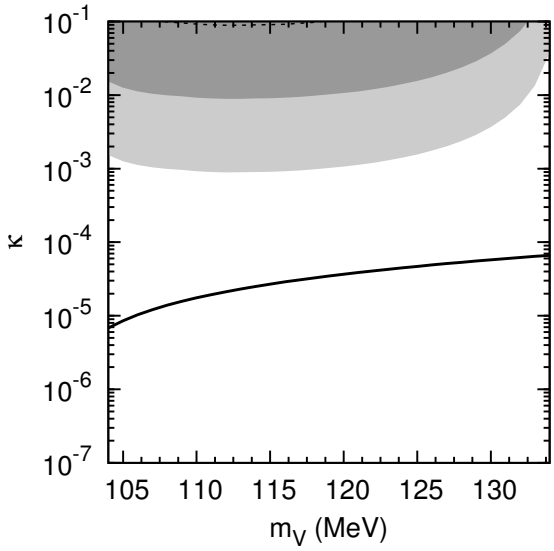

(c) $m_\chi = 50$ MeV

Figure 4.3: Expected number of neutral current-like dark matter nucleon scattering events at the MiniBooNE detector for three values of m_χ. These plots include only the contributions from π^0 decays. The regions show greater than 10 (light), 1000 (medium) and 10^6 (dark) expected events. The dotted line marks 10^5 events, corresponding to the number of elastic neutral current nucleon scattering events observed by MiniBooNE. Areas below the black line correspond to $\alpha' > 4\pi$.

a large bump that falls off sharply as $m_V \to m_\pi^0$. The η results are approximately an order of magnitude weaker than the pion results, which is more or less what we would expect from the ratio of N_{π^0} to N_η discussed in section 3.3.2. The sensitivity also falls off at large values of m_V as the drop in phase space begins to suppress $\mathrm{Br}_{\eta\to V\gamma}$. We see drops in sensitivity as we increase m_χ quite similar to those seen in the earlier π^0-only production channel analysis. As with the previous MiniBooNE electron scattering analysis, we cannot use these results to constrain the parameter space for lack of an experimental analysis with which we could compare our results, and so they are an optimistic assessment of MiniBooNE's sensitivity to hidden sector dark matter through scattering between dark matter and electrons. While we did extend the analysis to $m_\chi = 100$ MeV, the sensitivity was so weak as to barely show up on the plot at all, and so we have chosen not to display those results here.

4.2.4 Dark Matter Nucleon Scattering From the π^0 and η Decay Channels

We now arrive at the most interesting results of our analysis, elastic neutral current-like scattering between nucleons and dark matter produced from both the π^0 and η decay channels, shown in Fig. 4.5. We begin with the $m_\chi = 1$ MeV case, which we have plotted over the range $m_V \in [4, 545]$ MeV in Fig 4.5a. We draw upon the MiniBooNE analysis results mentioned earlier, and are able to safely exclude regions of the parameter space for which we would predict more than 10^5 events (still shown by a dashed line). This includes the entire darkly shaded region and around a third of the medium region. One interesting feature to note is that for the nucleon scattering, the sensitivity gradually grows as we increase m_V, at least until it is suppressed by $\mathrm{Br}_{\eta\to V\gamma}$. The sensitivity due to the η decay channel for $m_V \sim 300$ MeV is actually of the same order of magnitude as that of the π^0 decay channel at $m_V \sim 100$ MeV. This slow trend of increasing sensitivity as the mass of the V grows comes about due to the expression we have chosen for the ratio $\alpha'\kappa^2/\alpha$ in equation (3.10). Thanks to the increasingly stringent strong coupling condition, we can exclude all of the parameter space above $m_V = 50$ MeV using the MiniBooNE results. By combining this exclusion with those from LSND, we can eliminate the entirety of the parameter space apart from perhaps the smallest values of m_V, likely eliminating this scenario entirely for $m_\chi \sim$ few MeV and ending any hope for it as a possible explanation of the 511 KeV line, at least in its current form.

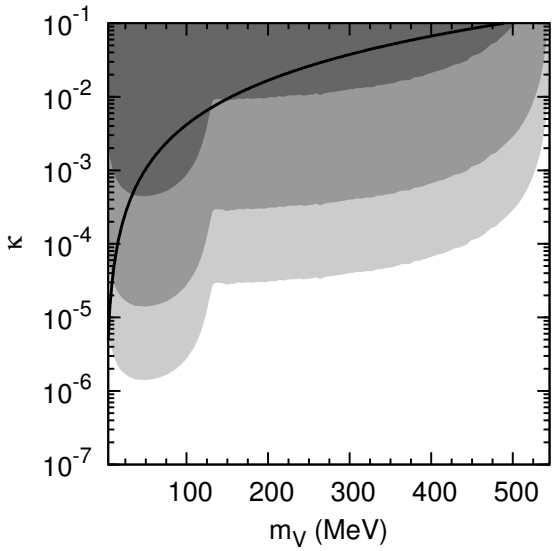

(a) $m_\chi = 1$ MeV

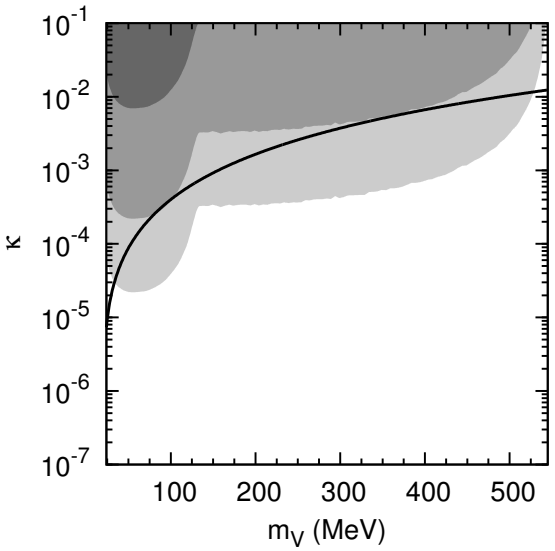

(b) $m_\chi = 10$ MeV

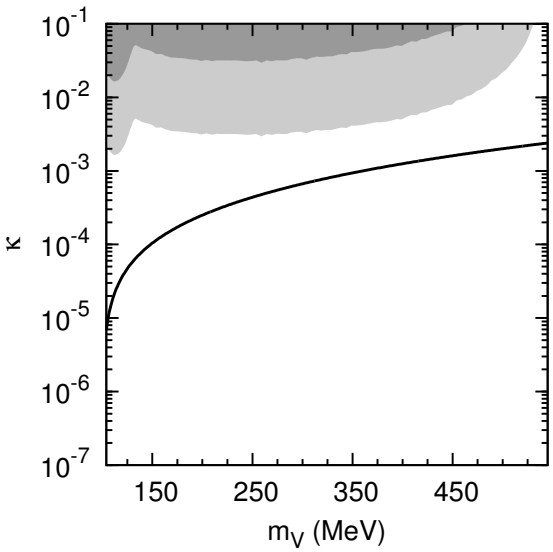

(c) $m_\chi = 50$ MeV

Figure 4.4: Expected number of neutral current-like dark matter electron scattering events at the MiniBooNE detector for three values of m_χ. These plots include the contributions from both π^0 and η decays. The regions show greater than 10 (light), 1000 (medium) and 10^6 (dark) expected events. Areas below the black line correspond to $\alpha' > 4\pi$.

The $m_\chi = 10$ MeV plot shown in Fig. 4.5b is also capable of ruling out large swathes of the parameter space, though not as thoroughly as the previous case. The sensitivity decreases by about an order of magnitude, as do the constraints from the strong coupling condition. However, combining these results with those from LSND in Fig. 4.1b eliminates some values of m_V completely while restricting the tightly restricting the κ range of most others. It is possible that future anti-neutrino data from MiniBooNE will allow us to eliminate the scenario altogether for $m_\chi \simeq 10$ MeV. We have also plotted the expected number of events for $m_\chi = 50$ MeV and $m_\chi = 100$ MeV in Figs. 4.5c and 4.5d. As expected from previous analyses, the sensitivity weakens considerably, and we are left with substantial non-excluded regions of the parameter space. It is worth noting at this point that, as with LSND, the kinematics of neutrino and dark matter beams differ markedly. Our constraints could therefore be be improved by using a spectral analysis to eliminate some of the 10^5 events observed by MiniBooNE which do not resemble dark matter scattering events.

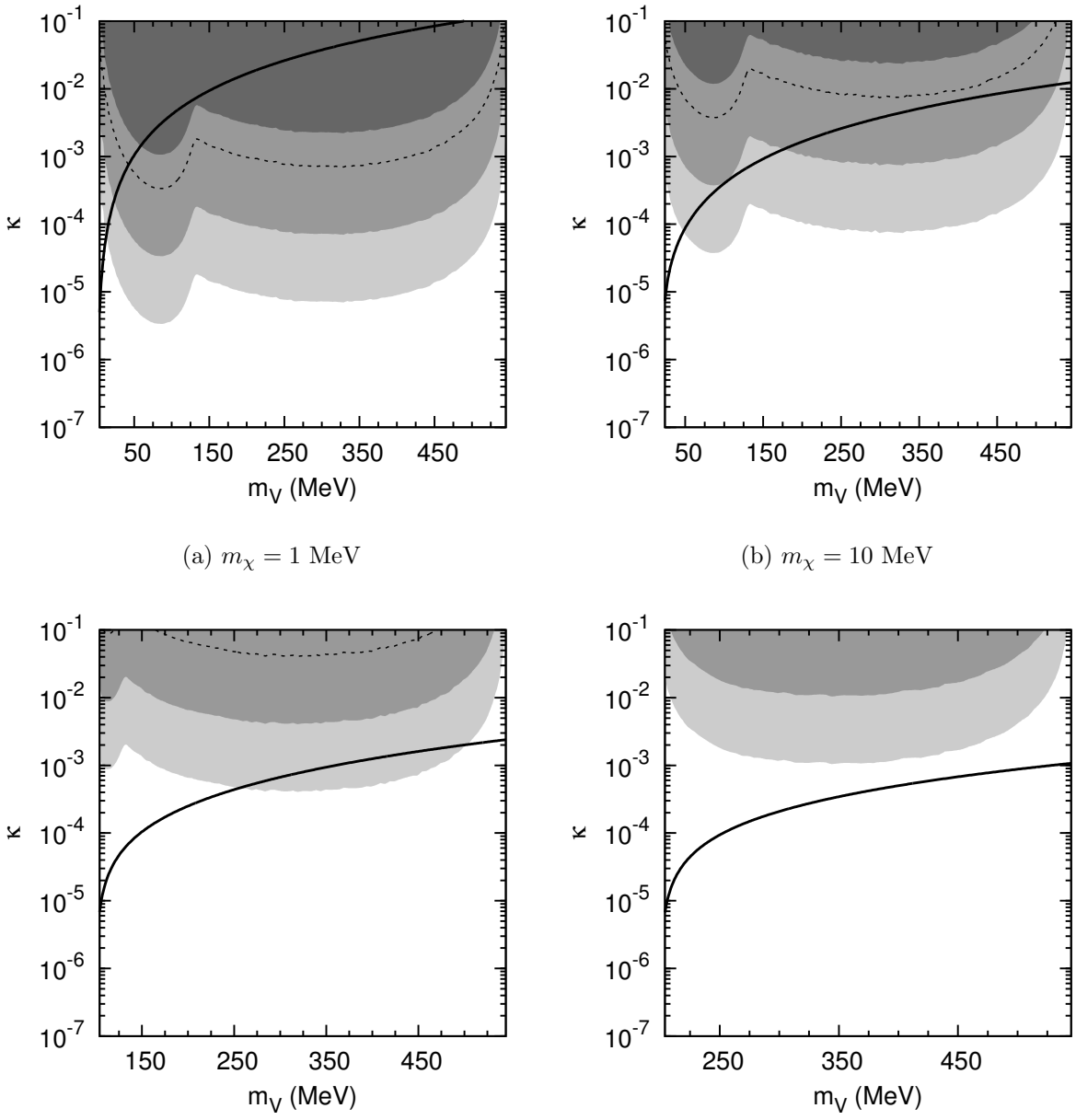

(a) $m_\chi = 1$ MeV

(b) $m_\chi = 10$ MeV

(c) $m_\chi = 50$ MeV

(d) $m_\chi = 100$ MeV

Figure 4.5: Expected number of neutral current-like dark matter nucleon scattering events at the MiniBooNE detector for four values of m_χ. These plots include the contributions from both π^0 and η decays. The regions show greater than 10 (light), 1000 (medium) and 10^6 (dark) expected events. The dotted line marks 10^5 events, corresponding to the number of elastic neutral current nucleon scattering events observed by MiniBooNE. Areas below the black line correspond to $\alpha' > 4\pi$.

Chapter 5

Conclusion

Our immediate goal in this project was to determine the sensitivity of two fixed target neutrino experiments to a hidden sector light dark matter scenario whose annihilations into Standard Model particles are mediated by a sub-GeV scale vector gauge boson. We found that between the results of MiniBooNE and LSND, we could probe large portions of the parameter space of the scenario for $\mathcal{O}$(MeV) dark matter. By combining the sensitivity of the experiments with the condition that dark matter should not be strongly self-interacting, we found that the $\mathcal{O}$(MeV) scenario was completely excluded as a viable dark matter candidate for $m_V > 2m_\chi$. While the sensitivity weakens as we increase the mass of the dark matter candidate, it was still strong enough for hidden sector dark matter masses as large as 10 MeV to rule out most of the parameter space, and determine that this hidden sector scenario was not a viable source for the 511 KeV gamma ray emission from the galactic bulge observed by the INTEGRAL satellite. While these experiments had some ability to probe the parameter space of 50 MeV and 100 MeV dark matter, the sensitivity was considerably weaker than for few MeV dark matter.

Under the hidden sector light dark matter scenario, a dark matter beam could be produced through the decays of the neutral mesons (η and π^0, specifically) that are copiously produced at fixed target neutrino experiments. These mesons are not a significant source of neutrinos or background for these experiments, and are normally ignored. We estimated the number produced by comparing their production with that of the far more closely studied charged pions. We wrote a Monte Carlo code to simulate the production of a dark matter beam at the MiniBooNE detector and determine the likelihood a dark matter particle would actually reach the detector and scatter in a manner detectable to the experiment. The results of the simulation

were used to calculate the expected number of events at each experiment over the parameter space of the scenario for four representative light dark matter masses: 1 MeV, 10 MeV, 50 MeV and 100 MeV. This code was then adapted to the LSND experiment, which had been previously studied, but the analysis of which could be extended to larger dark matter masses, as well as being used to double check the accuracy of the simulation.

While our immediate objective was to test the sensitivity of MiniBooNE and LSND to one particular dark matter candidate, a more long term interest is in the ability of fixed target experiments like MiniBooNE and LSND to probe other low mass states that are difficult to otherwise detect. The sensitivity of underground direct dark matter detection experiments weakens drastically for masses below 10 GeV, and any complementary search channel which allows us to access these masses would be invaluable to our current search for a non-gravitational dark matter signal. While the mass reach of LSND and MiniBooNE is likely limited to sub-GeV scale states, experiments with considerably larger proton beam energies such as MINOS and T2K are now producing results and analyses which should allow them access to states as large as a few GeV. We conclude that adding fixed target experiments to the current array of dark matter searches could allow for a more complete coverage of the range of dark matter masses.

Bibliography

[1] K. G. Begeman, A. H. Broeils, and R. H. Sanders. Extended rotation curves of spiral galaxies: Dark haloes and modified dynamics. *Mon. Not. Roy. Astron. Soc.*, 249:523, 1991.

[2] The CDMS II Collaboration. Dark Matter Search Results from the CDMS II Experiment. *Science*, 327(5973):1619–1621, 2010.

[3] E. Aprile et al. Dark Matter Results from 100 Live Days of XENON100 Data. *Phys.Rev.Lett.*, 2011.

[4] Pierre Jean, J. Knodlseder, W. Gillard, N. Guessoum, K. Ferriere, et al. Spectral analysis of the Galactic e^+ e^- annihilation emission. *Astron.Astrophys.*, 445:579–589, 2006.

[5] A. Aguilar et al. Evidence for Neutrino Oscillations from the Observation of $\bar{\nu}_e$ Appearance in a $\bar{\nu}_\mu$ Beam. *Phys.Rev.*, D64:112007, 2001.

[6] A.A. Aguilar-Arevalo et al. The MiniBooNE Detector. *Nucl.Instrum.Meth.*, A599:28–46, 2009.

[7] N. Prantzos, C. Boehm, A.M. Bykov, R. Diehl, K. Ferriere, et al. The 511 keV emission from positron annihilation in the Galaxy. 2010. arXiv:1009.4620 [astro-ph.HE].

[8] Celine Boehm, Dan Hooper, Joseph Silk, Michel Casse, and Jacques Paul. MeV Dark Matter: Has it Been Detected? *Phys.Rev.Lett.*, 92:101301, 2004.

[9] Benjamin W. Lee and Steven Weinberg. Cosmological Lower Bound on Heavy Neutrino Masses. *Phys.Rev.Lett.*, 39:165–168, 1977.

[10] C. Boehm and Pierre Fayet. Scalar Dark Matter candidates. *Nucl.Phys.*, B683:219–263, 2004.

[11] Pierre Fayet. Light spin-$\frac{1}{2}$ or spin-0 Dark Matter particles. *Phys. Rev.*, D70:023514, 2004.

[12] Pierre Fayet. Constraints on Light Dark Matter and U bosons, from ψ, Υ, K^+, π^0, η and η' decays. *Phys. Rev.*, D74:054034, 2006.

[13] Pierre Fayet. U-boson production in e^+ e^- annihilations, ψ and Υ decays, and Light Dark Matter. *Phys.Rev.*, D75:115017, 2007.

[14] Maxim Pospelov, Adam Ritz, and Mikhail B. Voloshin. Secluded WIMP Dark Matter. *Phys.Lett.*, B662:53–61, 2008.

[15] Dan Hooper and Kathryn M. Zurek. A Natural Supersymmetric Model with MeV Dark Matter. *Phys.Rev.*, D77:087302, 2008.

[16] Brian Batell, Maxim Pospelov, and Adam Ritz. Exploring Portals to a Hidden Sector Through Fixed Targets. *Phys.Rev.*, D80:095024, 2009.

[17] Natalia Borodatchenkova, Debajyoti Choudhury, and Manuel Drees. Probing MeV Dark Matter at Low-Energy e^+ e^- Colliders. *Phys. Rev. Lett.*, 96:141802, 2006.

[18] Maxim Pospelov. Secluded U(1) below the weak scale. *Phys.Rev.*, D80:095002, 2009.

[19] Brian Batell, Maxim Pospelov, and Adam Ritz. Probing a Secluded U(1) at B-factories. *Phys. Rev.*, D79:115008, 2009.

[20] Rouven Essig, Philip Schuster, and Natalia Toro. Probing Dark Forces and Light Hidden Sectors at Low-Energy e^+e^- Colliders. *Phys.Rev.*, D80:015003, 2009.

[21] Matthew Reece and Lian-Tao Wang. Searching for the light dark gauge boson in GeV-scale experiments. *JHEP*, 0907:051, 2009.

[22] Rouven Essig, Roni Harnik, Jared Kaplan, and Natalia Toro. Discovering New Light States at Neutrino Experiments. *Phys.Rev.*, D82:113008, 2010.

[23] James D. Bjorken, Rouven Essig, Philip Schuster, and Natalia Toro. New Fixed-Target Experiments to Search for Dark Gauge Forces. *Phys.Rev.*, D80:075018, 2009.

[24] Rouven Essig, Philip Schuster, Natalia Toro, and Bogdan Wojtsekhowski. An Electron Fixed Target Experiment to Search for a New Vector Boson A' Decaying to e^+e^-. *JHEP*, 1102:009, 2011. arXiv:1001.2557 [hep-ph].

[25] James D. Bjorken, Rouven Essig, Philip Schuster, and Natalia Toro. New Fixed-Target Experiments to Search for Dark Gauge Forces. *Phys.Rev.*, D80:075018, 2009.

[26] Gerard Jungman, Marc Kamionkowski, and Kim Griest. Supersymmetric Dark Matter. *Phys. Rept.*, 267:195–373, 1996.

[27] Gianfranco Bertone, Dan Hooper, and Joseph Silk. Particle Dark Matter: Evidence, Candidates and Constraints. *Phys.Rept.*, 405:279–390, 2005.

[28] Dan Hooper. TASI 2008 Lectures on Dark Matter. 2009. arXiv:0901.4090 [hep-ph].

[29] Gianfranco Bertone. *Particle Dark Matter: Observations, Models and Searches*. Cambridge Univ. Press, Cambridge, 2010.

[30] K. Nakamura et al. Review of particle physics. *J.Phys.G*, G37:075021, 2010.

[31] Annamaria Borriello and Paolo Salucci. The dark matter distribution in disk galaxies. *Mon. Not. Roy. Astron. Soc.*, 323:285, 2001.

[32] Henk Hoekstra, Howard Yee, and Mike Gladders. Current status of weak gravitational lensing. *New Astron. Rev.*, 46:767–781, 2002.

[33] Mario Mateo. Dwarf galaxies of the Local Group. *Ann.Rev.Astron.Astrophys.*, 36:435–506, 1998.

[34] Dennis Zaritsky, Rodney Smith, Carlos Frenk, and Simon D.M. White. More Satellites of Spiral Galaxies. *Astrophys.J.*, 478:39–48, 1997.

[35] F. Zwicky. Spectral displacement of extra galactic nebulae. *Helv.Phys.Acta*, 6:110–127, 1933.

[36] Neta A. Bahcall and Xiao-hui Fan. The Most Massive Distant Clusters: Determining Ω and σ_8. *Astrophys.J.*, 504:1, 1998.

[37] A. Kashlinsky. Determining Ω from cluster correlation function. *Phys.Rept.*, 307:67–73, 1998.

[38] Douglas Clowe, Marusa Bradac, Anthony H. Gonzalez, Maxim Markevitch, Scott W. Randall, et al. A direct empirical proof of the existence of dark matter. *Astrophys.J.*, 648:L109–L113, 2006.

[39] E. Komatsu et al. Five-Year Wilkinson Microwave Anisotropy Probe (WMAP) Observations: Cosmological Interpretation. *Astrophys.J.Suppl.*, 180:330–376, 2009.

[40] J. Dunkley et al. Five-Year Wilkinson Microwave Anisotropy Probe (WMAP) Observations: Likelihoods and Parameters from the WMAP data. *Astrophys. J. Suppl.*, 180:306–329, 2009.

[41] Keith A. Olive. TASI Lectures on Dark Matter. pages 797–851, 2003. arXiv:0301505 [astro-ph].

[42] Pasquale Dario Serpico and Georg G. Raffelt. MeV-mass dark matter and primordial nucleosynthesis. *Phys. Rev.*, D70:043526, 2004.

[43] Max Tegmark et al. Cosmological parameters from SDSS and WMAP. *Phys.Rev.*, D69:103501, 2004.

[44] E. Behnke, J. Behnke, S.J. Brice, D. Broemmelsiek, J.I. Collar, et al. Improved Limits on Spin-Dependent WIMP-Proton Interactions from a Two Liter CF_3I Bubble Chamber. *Phys.Rev.Lett.*, 106:021303, 2011.

[45] H.S. Lee et al. Limits on WIMP-nucleon cross section with CsI(Tl) crystal detectors. *Phys.Rev.Lett.*, 99:091301, 2007.

[46] Marie-Cecile Piro. Status of the PICASSO experiment for spin-dependent Dark Matter searches. 2010. arXiv:1005.5455 [astro-ph.IM].

[47] R. Bernabei et al. First results from DAMA/LIBRA and the combined results with DAMA/NaI. *Eur.Phys.J.*, C56:333–355, 2008.

[48] Lars Bergstrom, Piero Ullio, and James H. Buckley. Observability of γ Rays from Dark Matter Neutralino Annihilations in the Milky Way Halo. *Astropart.Phys.*, 9:137–162, 1998.

[49] N.W. Evans, F. Ferrer, and Subir Sarkar. A "Baedecker" for the Dark Matter Annihilation Signal. *Phys.Rev.*, D69:123501, 2004.

[50] Lars Bergstrom and Dan Hooper. Dark Matter and Gamma-Rays from Draco: MAGIC, GLAST and CACTUS. *Phys.Rev.*, D73:063510, 2006.

[51] Piero Ullio, Lars Bergstrom, Joakim Edsjo, and Cedric G. Lacey. Cosmological dark matter annihilations into γ-rays - a closer look. *Phys.Rev.*, D66:123502, 2002.

[52] M. Casse, B. Cordier, J. Paul, and Stephane Schanne. Hypernovae / GRB in the Galactic Center as possible sources of Galactic Positrons. *Astrophys.J.*, 602:L17–L20, 2004.

[53] Georg Weidenspointner, Gerry Skinner, Pierre Jean, Jurgen Knodlseder, Peter von Ballmoos, et al. An asymmetric distribution of positrons in the Galactic disk revealed by γ-rays. *Nature*, 451:159–162, 2008.

[54] John F. Beacom and Hasan Yuksel. Stringent Constraint on Galactic Positron Production. *Phys.Rev.Lett.*, 97:071102, 2006.

[55] Oscar Adriani et al. An anomalous positron abundance in cosmic rays with energies 1.5-100 GeV. *Nature*, 458:607–609, 2009.

[56] C. Boehm, T. A. Ensslin, and J. Silk. Can annihilating dark matter be lighter than a few GeV? *J. Phys.*, G30:279–286, 2004.

[57] Brian Patt and Frank Wilczek. Higgs-field portal into hidden sectors. arXiv:hep-ph/0605188.

[58] Robert Foot and Xiao-Gang He. Comment on Z-Z$'$ mixing in extended gauge theories. *Phys.Lett.*, B267:509–512, 1991.

[59] D.G. Cerdeno, A. Dedes, and T.E.J. Underwood. The Minimal Phantom Sector of the Standard Model: Higgs Phenomenology and Dirac Leptogenesis. *JHEP*, 0609:067, 2006.

[60] Markus Ahlers, Joerg Jaeckel, Javier Redondo, and Andreas Ringwald. Probing Hidden Sector Photons through the Higgs Window. *Phys.Rev.*, D78:075005, 2008.

[61] Jonathan L. Feng, Huitzu Tu, and Hai-Bo Yu. Thermal Relics in Hidden Sectors. *JCAP*, 0810:043, 2008.

[62] Pierre Fayet, Dan Hooper, and Gunter Sigl. Constraints on Light Dark Matter From Core-Collapse Supernovae. *Phys.Rev.Lett.*, 96:211302, 2006.

[63] C. Athanassopoulos et al. The Liquid Scintillator Neutrino Detector and LAMPF Neutrino Source. *Nucl.Instrum.Meth.*, A388:149–172, 1997.

[64] A.A. Aguilar-Arevalo et al. The Neutrino Flux prediction at MiniBooNE. *Phys.Rev.*, D79:072002, 2009.

[65] A.A. Aguilar-Arevalo et al. Measurement of the Neutrino Neutral-Current Elastic Differential Cross Section on Mineral Oil at $E_\nu \sim 1$ GeV. *Phys.Rev.*, D82:092005, 2010.

[66] S. Teis et al. Pion-Production in Heavy-Ion Collisions at SIS energies. *Z. Phys.*, A356:421–435, 1997.

[67] Michel Sorel. Search for Sterile Neutrinos Using the MiniBooNE Beam. 2005. FERMILAB-THESIS-2005-07.

[68] R L Burman and E S Smith. Parameterization of Pion Production and Reaction Cross Sections at LAMPF Energies. Technical Report LA-11502-MS. DE-98-011120. UC-414, Los Alamos Nat. Lab., Los Alamos, NM, 1989.

[69] L. B. Auerbach et al. Measurement of electron-neutrino electron elastic scattering. *Phys. Rev.*, D63:112001, 2001.

[70] L.A. Ahrens, S.H. Aronson, P.L. Connolly, B.G. Gibbard, M.J. Murtagh, et al. Measurement of neutrino-proton and antineutrino- proton elastic scattering. *Phys.Rev.*, D35:785, 1987.